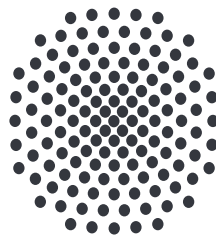


# Fast Magnetic Field Control for the Precise Tuning of Interactions in a Dipolar Gas

Master Thesis

Carl Matthias Bühner

November 17, 2017



**Universität Stuttgart**

5. Physikalisches Institut

Hauptberichter: Prof. Dr. Tilman Pfau

Mitberichter: Prof. Dr. Jörg Wrachtrup

# Contents

<b>1</b>	<b>Zusammenfassung (german)</b>	<b>2</b>
<b>2</b>	<b>Introduction</b>	<b>4</b>
<b>3</b>	<b>Theoretical Framework</b>	<b>6</b>
3.1	Contact Interaction . . . . .	6
3.2	Feshbach Resonances . . . . .	8
3.3	Dipole-Dipole Interaction . . . . .	9
3.4	Tuning the Dipole-Dipole Interaction . . . . .	10
3.5	BEC & Droplets . . . . .	12
<b>4</b>	<b>Improvement of the Magnetic Field</b>	<b>14</b>
4.1	Curvature and Strength of the Magnetic Field . . . . .	16
4.2	Impedance and LCR Circuits . . . . .	20
<b>5</b>	<b>Magnetic Shielding</b>	<b>28</b>
<b>6</b>	<b>Rotating Quantum Droplets</b>	<b>37</b>
6.1	Dysprosium . . . . .	37
6.2	Experimental Setup . . . . .	37
6.3	Rotating Quantum Droplets . . . . .	40
<b>7</b>	<b>Summary and Outlook</b>	<b>43</b>

# 1 Zusammenfassung (german)

Im Jahr 1995 wurden die ersten Bose-Einstein-Kondensate (BEC) mit Natrium-  
atomen [1] und Rubidiumatomen [2] realisiert. Bosonen unterliegen im Gegensatz  
zu Fermionen nicht dem Pauli-Prinzip und können sich somit alle im Grundzustand  
befinden. Hierfür sind allerdings sehr geringe Temperaturen nötig. Mit Hilfe der La-  
serkühlung werden die Atome auf die Doppler-Temperatur [3] heruntergekühlt und  
dann mittels Verdampfungskühlung [4] unter die kritische Temperatur gebracht.  
Mit letzterer werden nur die heißesten Atome aus der Wolke entfernt, wodurch die  
Atomwolke nach der Thermalisierung immer kälter wird. Seitdem wurden viele ver-  
schiedene Elemente kondensiert, Alkaliatome wie Rubidium, sowie Erdalkalimetalle  
wie Strontium [5]. Eine weitere Klasse von Elementen sind Chrom [6], Dysprosium [7]  
und Erbium [8], welche deutlich größere magnetische Momente besitzen. Durch das  
große magnetische Moment  $\mu_r \approx 10$  und der dadurch starken Dipol-Dipol Wech-  
selwirkung reagieren diese Atome sehr empfindlich auf externe Magnetfelder. So  
ändert sich wegen der dipolaren Wechselwirkung zum Beispiel das Seitenverhältnis  
eines BEC, was Magnetostriktion genannt wird [9]. Bei hohen Dichten beschreibt  
die Molekularfeldtheorie den stabilen Zustand des Quanten-Gases nicht mehr, da  
Quantenfluktuationen berücksichtigt werden müssen. In dem, in dieser Arbeit be-  
schriebenen, Experiment werden Dysprosiumatome verwendet.

Außer der dipolaren Wechselwirkung gibt es auch noch die Kontakt-Wechsel-  
wirkung aufgrund von Stößen zwischen den einzelnen Atomen. Das Verhältnis der  
Stärke zwischen der dipolaren und der Kontakt-Wechselwirkung wird  $\epsilon_{dd}$  bezeichnet.  
Es ist möglich, die Kontakt-Wechselwirkung mittels einer Feshbachresonanz durch-  
zustimmen. Hierfür muss die Stärke des Magnetfelds variiert werden. Seit 2002 gibt  
es einen Ansatz, der zeigt, dass es grundsätzlich möglich ist im zeitlichen Mittel die  
dipolare Wechselwirkung zu variieren [10]. Dabei wird das Magnetfeld unter einen  
Winkel  $\phi$  rotiert (Siehe Abbildung 3). Um von einem zeitlichen Mittel sprechen zu  
können, muss das Magnetfeld relativ schnell rotieren. Weiterhin muss es möglich  
sein, zusätzlich eine statische Komponente orthogonal anlegen zu können [10].

Aus diesem wurde eine neue Spulenanordnung entwickelt und getestet. Die neue  
Spulenanordnung besteht aus einem Spulenpaar in z-Richtung, das in Helmholtz-  
Anordnung ist und somit ein relativ konstantes Magnetfeld ermöglicht und zusätz-

lich zwei Spulenpaaren entlang der Raumdiagonalen in der  $xy$ -Ebene. Aufgrund von Platzmangel war die Helmholtz-Anordnung für die  $xy$ -Spulen nicht praktikabel und die Spulen wurden mit großem Abstand zueinander befestigt, was zu einer merklichen Krümmung des Magnetfeldes führt. Allerdings ist der Gradient des Magnetfeldes noch so klein, dass die Atome nicht aus der optischen Dipolfalle gezogen werden oder die Feshbachresonanz nicht mehr zu verwenden ist. Dies gilt vor allem da nach dem Kühlen die Atomwolke viel kleiner ist und somit nur einen kleinen Gradienten sieht. Mit den verwendeten Netzgeräten lassen sich mit allen Spulenpaaren Magnetfelder von 8 G erzeugen. Um die Stärke der Dipol-Dipol Wechselwirkung zu variieren, muss das Magnetfeld schnell rotieren. Da die  $xy$ -Spulen allerdings eine relativ hohe Impedanz haben, muss ein Schwingkreis verwendet werden, um das Magnetfeld bei einer Frequenz von 5 kHz zu treiben. Mit Folienkondensatoren ist dies möglich und das Feld lässt sich rotieren, wenn die  $x$ - und die  $y$ -Spulenpaare phasenverschoben betrieben werden. Die verwendeten Feshbachresonanzen haben eine Breite von einigen mG, weshalb das Magnetfeld sehr genau bestimmt sein muss. Um statische Felder, wie das Erdmagnetfeld, zu kompensieren, sind im aktuellen Aufbau Kompensationsspulen in Verwendung. Diese können das Magnetfeld im Bereich von mG kompensieren. Um zu noch niedrigeren Feldern zu kommen, muss das Magnetfeld anders geschirmt werden, zum Beispiel mit Mu-Metall. In dieser Arbeit wurde gezeigt, dass ein geschlossener Kasten sinnvoll ist und schon eine 0.1 mm dicke Folie zu einem Schirmfaktor von bis zu 20 führt.

Der abschließende Teil dieser Arbeit ist die Beobachtung von Quanten-Tröpfchen [11] in einem rotierenden Magnetfeld. Dabei rotiert das Tröpfchen mit dem Magnetfeld ohne sichtbare Verzögerung. Mit höheren Frequenzen steigt der Effekt des Zentrifugalpotentials, was die Lebensdauer des Tröpfchens stark verkürzt. Auch deuten Messungen darauf hin, dass es möglich ist Tröpfchen schneller als die transversalen Fallenfrequenzen zu rotieren, der die selbstbindende Wirkung [12] des Tröpfchens zeigt. Mit den neuen Spulen ist es auch möglich schneller zu rotieren und so weitere Effekte zu entdecken.

## 2 Introduction

In 1908 it was for the first time possible to reach very cold temperatures of about 4 K where the first liquefaction of helium happened [13]. At this temperature quantum mechanical effects were observed. For example mercury becomes superconducting [13] and helium can enter a superfluid phase [14, 15]. Superfluidity was understood to be the manifestation of the phenomena of Bose-Einstein condensation (BEC). But because of strong interactions in superfluid helium, a direct identification of a BEC could not be made. It took almost a century time and the development of efficient laser cooling mechanisms until the first weakly interacting BEC was realized 1995 for sodium atoms [1] and rubidium atoms [2]. With laser cooling the atoms were cooled down to the Doppler limit [3] and then below the critical temperature by evaporative cooling [4]. Since then many different atoms have been condensed, alkali metals like two rubidium isotopes [2, 16], lithium [17], potassium [18] and cesium [19], as well as alkaline earth metals like strontium [5]. Another class of elements are chromium [6], dysprosium [7] and erbium [8], which feature large magnetic moments. These atoms are sensitive to magnetic fields and the dipole-dipole interaction between the atoms is not negligible. In 2005 the element chromium was first condensed in our group giving rise to the observation of dipolar effects in BECs [6]. It was shown that it is possible to experimentally tune the ratio of dipole-dipole to contact interactions [20].

In chromium the dipolar interaction is only a small perturbation in terms of strength compared to the contact interaction. By tuning the contact interaction via Feshbach resonances this could be changed, but this also leads to high three-body losses.

With the condensation of atoms with even stronger magnetic dipole moments, like dysprosium [7] and erbium [8], strong dipolar effects are now possible without tuning the contact interaction to small values. Dysprosium is a rare earth metal with a magnetic moment of  $\mu_m \approx 10 \mu_B$  and the strength of the dipolar interaction  $a_{dd} \approx 132 a_0$  is larger than of the contact interaction  $a_s = 92(8) a_0$ . The dipole-dipole interaction is anisotropic and has a long-range behavior. This interaction can be repulsive or attractive depending on the trap geometry due to the anisotropy. BECs are only stable for repulsive interactions, but collapse for attractive interactions [21].

Such a collapse was observed with chromium [22], where the interplay of contact and dipolar interactions revealed a rich stability diagram that depends on the ratio of attractive and repulsive interactions and therefore the trap geometry [23]. For dysprosium this collapse leads to a new stable phase, so called quantum droplets [11, 24–27].

For better understanding the thesis will first give a short introduction into the theoretical framework of dipolar BEC. For example, in 2002 there was a proposal to tune the magnitude and sign of the dipolar interaction via a rotating magnetic field [10], which has not been realized so far due to technical limitations [28]. The next chapter covers the development and construction of a setup of coils to generate versatile magnetic fields in arbitrary directions. The shielding of static magnetic fields, which is described in chapter 5, is necessary for controlled contact and dipolar interaction. Additionally, we will show how such a field can be used to rotate quantum droplets to reveal subtle properties of their collective many-body behavior. A short summary and outlook will conclude this thesis.

### 3 Theoretical Framework

Our goal is to study the behavior of ultra-cold atom gases. Accessible to our experiment is the time-resolved atom distribution, therefore it is interesting to predict the states and the dynamics of ultra-cold gases. The fundamental terms to the microscopic Hamiltonian are the kinetic energy and the interaction between the particles. In the ultra-cold regime the atoms have less momentum than at higher temperatures, so the interactions play a larger role compared to the influence of the kinetic energy. Therefore the atom distribution of bosons is not a thermal Boltzmann distribution but a Bose-Einstein distribution [21]. Because of this we now consider the interactions in the ultra-cold regime, which include two types of interactions, contact interactions (CI) and dipole-dipole interactions (DDI) which will be explained in the following chapter. Alkali elements mainly have contact interactions, because they have just one unpaired electron with vanishing angular momentum in their outer electron shell, so their magnetic moments are small. Therefore the DDI is negligible [29]. Rare earth elements are different, they can have dominant dipole-dipole interactions due to higher magnetic moments.

#### 3.1 Contact Interaction

In atomic physics the short range and isotropic contact interaction is necessary to understand the dynamics of atom gases [30]. The contact interaction arises from attractive Van-der-Waals (VdW) forces and Coulomb repulsion due to the overlapping electron orbits. This leads to a Lennard-Jones potential. The VdW part scales with the distance  $r$  between the particle as  $-1/r^6$  and the Coulomb part with  $1/r^{12}$ . Therefore the potential has short range character. The interaction distance  $r_0$  is defined as the maximal distance, where the atoms feel the Lennard-Jones potential. The mean inter-atomic distance is much larger than the interaction distance  $r_0$ , so the atoms move almost freely. In ultra-cold atom gases the atoms have low kinetic energy. At a scattering event the particles transfer angular momentum  $l$ :  $\hbar l = m_{red} v r_{impact}$  with the Planck constant  $\hbar$ , the reduced mass  $m_{red}$ , the relative velocity of particles  $v$  and the distance  $r_{impact}$  (see figure 1). The de-Broglie wavelength of the two particles in the ultra-cold regime can be approximated as:

$\lambda_{dB} \equiv h/p \approx h/(m_{red}v)$ . Thus the angular momentum is:  $l = 2\pi r_{impact}/\lambda_{dB} \leq 2\pi r_0/\lambda_{dB}$ . In the ultra-cold regime (temperatures less than  $\mu\text{K}$ ) the de-Broglie wavelength is much larger than the interaction radius  $r_0$ . The angular momentum is quantized, therefore the only possible solution is  $l = 0$ . Solutions with  $l = 0$  are called s-wave. Since  $\lambda_{dB} \gg r_0$  the details of the potential are not resolved by the colliding atomic wave packets, the potential can be simplified and only a single parameter matters: the scattering length  $a$ . This scattering length comes from a phase shift of the wave packets. A process with hard classical spheres with radius  $a$  would have the same scattering cross section [30].

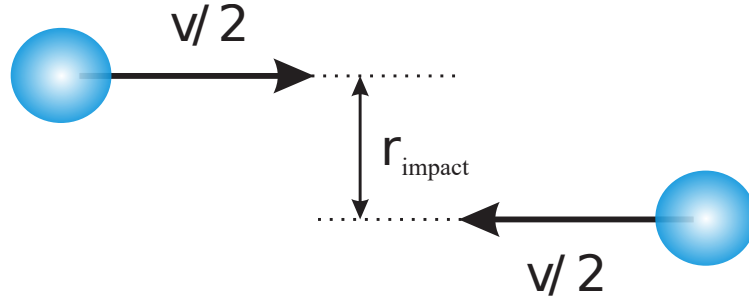


Figure 1: Two particles collide if the distance  $r_{impact}$  between them is smaller than  $r_0$ . Figure taken from [31].

A positive  $a$  leads to a repulsive potential and a negative scattering length to an attractive potential, although a negative scattering length does not have a classical analogue. The pseudo potential is given by [30]:

$$U_c(\mathbf{r}) = \frac{4\pi\hbar^2 a}{m} \delta(\mathbf{r}) = g\delta(\mathbf{r}), \quad (1)$$

where  $m$  is the mass of the atoms,  $\hbar$  the Planck constant and  $\delta(\mathbf{r})$  the Delta function.

## 3.2 Feshbach Resonances

The scattering length  $a$  is given by the phase shift which is determined by the details of the potential. In particular, when a bound-state solution near zero energy exists, the scattering length is divergent. A Feshbach resonance occurs when a parameter is varied so that the energy of a bound state can cross zero. This is possible using the Zeeman effect and coupling to another spin channel. More details of the Feshbach resonances can be found in [32]. The important term is the dependency of the scattering length on the magnetic field (see also figure 2):

$$a(B) = a_{bg} \left( 1 - \frac{\Delta B}{B - B_0} \right), \quad (2)$$

with  $a_{bg}$  the background scattering length far away from the Feshbach resonances,  $\Delta B$  the width and  $B_0$  the position of the resonances.

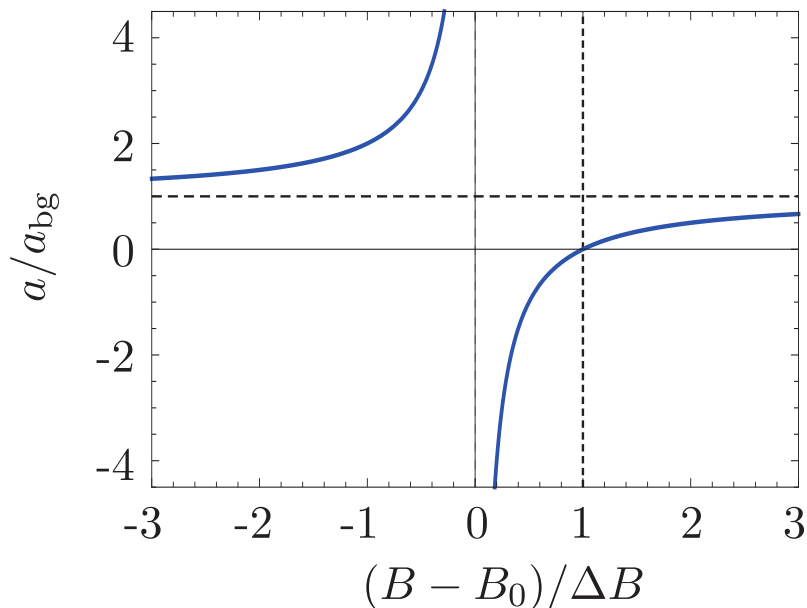


Figure 2: Scattering length dependency of the magnetic field detuning. For  $B = B_0$  the bound state is on resonance with the atoms. The horizontal dashed line symbolizes the background scattering length and the vertical dashed line represents the magnetic field for  $a = 0$ . Figure taken from [31].

### 3.3 Dipole-Dipole Interaction

Some rare earth atoms, like dysprosium or erbium, have non-negligible dipolar interactions because of their high magnetic moment ( $\mu_m$ ). In our experiments we work with external magnetic fields that polarize the atomic spins. The dipole-dipole potential is given as [10]:

$$U_{dd}(\mathbf{r}, t) = -\frac{\mu_0}{4\pi} \frac{(\boldsymbol{\mu}_m \cdot \hat{\mathbf{r}})(\boldsymbol{\mu}_m \cdot \hat{\mathbf{r}}) - (\boldsymbol{\mu}_m \cdot \boldsymbol{\mu}_m)}{r^3}, \quad (3)$$

with  $\boldsymbol{\mu}_m$  the magnetic moment of the atoms, the unit vector of the distance  $\hat{\mathbf{r}} = \frac{\mathbf{r}_1 - \mathbf{r}_2}{|\mathbf{r}_1 - \mathbf{r}_2|}$  and  $\mu_0$  the vacuum permeability. After spin polarization all dipoles align in the direction of the field:

$$U_{dd}(\mathbf{r}, t) = -\frac{\mu_0 \mu_m^2}{4\pi} \frac{3(\hat{\mathbf{e}}(t) \cdot \hat{\mathbf{r}})^2 - 1}{r^3}, \quad (4)$$

with  $\hat{\mathbf{e}}(t)$  the direction of the magnetic field. If one has a static magnetic field this leads to:

$$U_{dd}(\mathbf{r}) = -\frac{\mu_0 \mu_m^2}{4\pi} \left( \frac{3 \cos^2 \theta - 1}{r^3} \right). \quad (5)$$

This interaction is anisotropic as one can see in the  $\theta$  dependence of the formula and has a long range scaling ( $\propto 1/r^3$ ). It can be attractive or repulsive depending on the angle  $\theta$ . At a "magic angle" of  $\theta = \arccos \sqrt{1/3} \approx 55^\circ$  this energy vanishes.

In our experiments both types of interactions (DDI and CI) are present. Therefore it is useful to define a ratio  $\epsilon_{dd}$  of physical constants and relevant system parameters that describe the relative strength of the CI and the DDI:

$$\epsilon_{dd} = \frac{m \mu_0 \mu_m^2}{12\pi \hbar^2 a} \quad (6)$$

For  $\epsilon_{dd} > 1$  the DDI dominates and can destabilize a BEC depending on the aspect ratio of the trapping potential.

### 3.4 Tuning the Dipole-Dipole Interaction

Following the idea of a paper by S. Giovanazzi et al. in 2002 [10] the strength and sign of the DDI can be controlled by a rotating external magnetic field. At high frequencies of the rotating magnetic field the potential of the DDI can be time-averaged and so the effective DDI vanishes for the right parameter. The approach in the proposal to rotate the magnetic field with an additional static component orthogonal to the rotating field. Because of the smaller setup we tried to figure out how to change the magnetic field with only two pairs of coils and a wipe movement. Therefore one could think about changing the magnetic field in the xy-plane:

$$\mathbf{B}(t) = B_0 \hat{\mathbf{e}}(t) = B_0[(a(t))\hat{\mathbf{x}} + b(t)\hat{\mathbf{y}}], \quad (7)$$

with  $B_0$  the amplitude of the magnetic field,  $\hat{\mathbf{e}}(t)$  the unity vector of the magnetic field direction,  $a(t), b(t)$  time dependent functions and  $\hat{\mathbf{x}}, \hat{\mathbf{y}}, \hat{\mathbf{z}}$  the unit vectors of the coordinates. The functions  $a(t)$  and  $b(t)$  have to be normalized so that  $a(t)^2 + b(t)^2 = 1$ . From this magnetic field it follows that  $(\hat{\mathbf{e}}(t) \cdot \hat{\mathbf{r}})^2 = \sin^2(\theta) f(a(t), b(t), \angle(\hat{\mathbf{r}}_y, \hat{\mathbf{r}}_x))$  with the the unit vector of the distance  $\hat{\mathbf{r}}$  in spherical coordinates and the polar angle theta  $\theta = \angle(\hat{\mathbf{z}}, \hat{\mathbf{r}})$ . The time average of this term must be  $1/3$  in order to achieve a vanishing effective dipole-dipole interaction, as it can be seen from formula 4

$$\frac{\Omega}{2\pi} \int_0^{\frac{2\pi}{\Omega}} \sin^2(\theta) f(t) dt = \sin^2(\theta) \frac{\Omega}{2\pi} \int_0^{\frac{2\pi}{\Omega}} f(t) dt. \quad (8)$$

But without some a priori knowledge of  $\theta$  it is not possible to reach  $1/3$  and  $\theta$  is generally dependent on the shape of the trap potential and the ordering of the atoms. Thus this method will not work for all cases and is therefore not really feasible for the experiment. The way given in the paper [10] to make the vanishing effective DDI possible is rotating the magnetic field around an axis by the angle  $\phi$ . This is shown in figure 3. The magnetic field vector is given by [10]:

$$\mathbf{B}(t) = B_0 \hat{\mathbf{e}}(t) = B_0(\cos(\phi)\hat{\mathbf{z}} + \sin\phi[\cos(\Omega t)\hat{\mathbf{x}} + \sin(\Omega t)\hat{\mathbf{y}}]), \quad (9)$$

where  $\sin(\Omega t)$  and  $\cos(\Omega t)$  describe the oscillations of the field.

To calculate the time averaged potential of the DDI formula 4 including the

magnetic field can be used [10]:

$$\langle U_{dd} \rangle = \frac{\Omega}{2\pi} \int_0^{2\pi} U_{dd}(\mathbf{r}, t) dt = -\frac{\mu_0 \mu_m^2}{4\pi} \left( \frac{3 \cos^2 \theta - 1}{r^3} \right) \left( \frac{3 \cos^2 \phi - 1}{2} \right). \quad (10)$$

The additional factor  $\left( \frac{3 \cos^2 \phi - 1}{2} \right)$  in comparison to a static magnetic field (formula 5) can be varied between 1 and  $-1/2$  by changing the angle  $\phi$  of the field to the rotation axis. Thus the effective DDI can be switched (for example from attractive to repulsive) or completely suppressed by going to the magic angle  $\phi = 55^\circ$ . For this method it is necessary that the rotation frequency of the magnetic field is high enough (faster than the trap frequencies to be able to use the time average, also see chapter 6.2) and at the same time much smaller than the Larmor frequency. The latter corresponds to the Zeeman splitting of  $f_{larmor} = \Delta E_{Zeeman}/\hbar$ . If the frequency of the magnetic field is higher than the Larmor frequency the dipoles cannot follow the field [10].

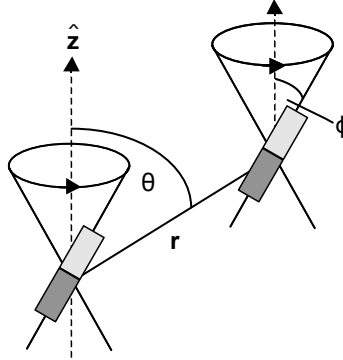


Figure 3: Two dipoles at a distance  $r$  and with an angle  $\theta$  when the magnetic field is applied in  $z$  direction. In this case there is an additional magnetic component spinning in the  $xy$ -plane, for tuning the interaction. Now the magnetic field is orientated with a certain angle  $\phi$  to the  $z$ -direction. Figure taken from [10].

The goal of this thesis is to set up a coil system that allows both, the use of a Feshbach resonance to tune the scattering length as well as is suitable for fast variations and oscillations of the field orientation to tune the DDI.

### 3.5 BEC & Droplets

Bosons are different in comparison to fermions, since they do not obey the Pauli principle. Thus at a low energy bosons can accumulate in the ground state. This is called a Bose-Einstein-Condensate (BEC). This requires low kinetic energies, which are equivalent to low temperatures. On a mean-field level the BEC wave function  $\psi(r)$  obeys the Gross-Pitaevskii equation (GPE) [21]:

$$\mu\psi(\mathbf{r}) = \left( \frac{\hbar^2\nabla^2}{2m} + V_{ext}(\mathbf{r}) + \Phi_{\text{contact}} + \Phi_{\text{dd}} \right) \psi(\mathbf{r}), \quad (11)$$

with the chemical potential  $\mu$ , the mean-field potential of the CI  $\Phi_{\text{contact}} = gn(\mathbf{r})$  and the mean-field potential of the DDI  $\Phi_{\text{dd}} = \int d^3r' U_{dd}(\mathbf{r} - \mathbf{r}')n(\mathbf{r}')$ , where the density is  $n = |\psi|^2$ .  $V_{ext}$  is the external potential, for which in our experimental setup, a harmonic trap, is a good approximation. In comparison to a Schrödinger equation the inter-atomic interactions introduce a nonlinearity.

The energy functional corresponding to formula 11 is:

$$E(n, \mathbf{r}) = \int d^3\mathbf{r} \left( \frac{\hbar^2\nabla^2}{2m} + V_{ext}(\mathbf{r}) + \frac{\Phi_{\text{contact}} + \Phi_{\text{dd}}}{2} \right) n(\mathbf{r}) \quad (12)$$

If the interaction part dominates over the kinetic energy (Thomas Fermi approximation [21]) the kinetic energy can be neglected. Using a variational ansatz one can calculate the interaction energy density by:

$$e_{MF} = \frac{gn_0^2}{2}(1 - \epsilon_{dd}f(\kappa)) \equiv \frac{gn_0^2}{2}\alpha \quad (13)$$

where  $n_0$  is the peak density,  $f(\kappa)$  a form factor depending on the aspect ratio  $\kappa$  of the BEC and  $\epsilon_{dd}$  the ratio between the strength of DDI and CI.

For  $\alpha < 0$  the system reduces its energy by increasing the peak density  $n_0$ , i.e., concentrating the many-body wavefunction in a smaller volume. This leads to a collapse of the BEC. This collapse is unphysical, as it leads to a divergence  $n \rightarrow \infty$  and so  $E \rightarrow -\infty$ . It means that the approximation underlying in formula 11 and 12 somehow break down. In particular the so-called mean-field approximation [21] is no longer verified. With the collapse the density increases and the beyond-mean-field

terms have to be taken into account. This term is called Lee-Huang-Yang (LHY) term which describes quantum fluctuations of phonon modes [33]:

$$e_{LHY} = \frac{gn_0^2}{2} \sqrt{n_0} \frac{128\sqrt{a^3}}{15\sqrt{\pi}} \left(1 + \frac{3}{2}\epsilon_{dd}^2\right) \equiv \frac{gn_0^2}{2} (\sqrt{n_0}\beta). \quad (14)$$

The LHY term is always larger than zero and leads to a repulsive interaction. The total interaction energy is given by the sum of the mean-field energy density and the LHY term:

$$e = \frac{gn_0^2}{2} (\alpha + \beta\sqrt{n_0}), \quad (15)$$

For negative alpha the system stabilizes at an equilibrium peak density given by  $\frac{\partial e}{\partial n} = 0$ :

$$n_0 \propto \left(\frac{\alpha}{\beta}\right)^2 \quad (16)$$

This density is independent of the atom number, like in a liquid. The relation is further independent of a trapping potential leading to self-bound solutions of the quantum droplet [12]. In conclusion the mean field solution predicts a collapse of the BEC, the LHY term can stabilize the system and a new liquid-like phase appears.

## 4 Improvement of the Magnetic Field

As mentioned in previous chapters we need magnetic fields to tune the contact and the DDI and to compensate the earth's magnetic field. The strength of the magnetic field is important, because of the magnetic field dependency of the CI due to Feshbach resonances. In  $^{164}\text{Dy}$  a Feshbach resonance exists at  $B_0 = 7.12\text{ G}$  with a width of  $\Delta B = 51\text{ mG}$ , and one at  $B_0 = 1.32\text{ G}$  and a width of  $\Delta B = 8\text{ mG}$  [11]. In the laboratory the magnetic field can be tuned to a maximum inaccuracy of  $3\text{ mG}$  due to accuracy of the electromagnets and the power supplies. So a large width is important for precise tuning of the scattering length. Due to the larger width  $\Delta B$  of the  $B_0 = 7.12\text{ G}$  resonance it is possible to get more atoms in the BEC.

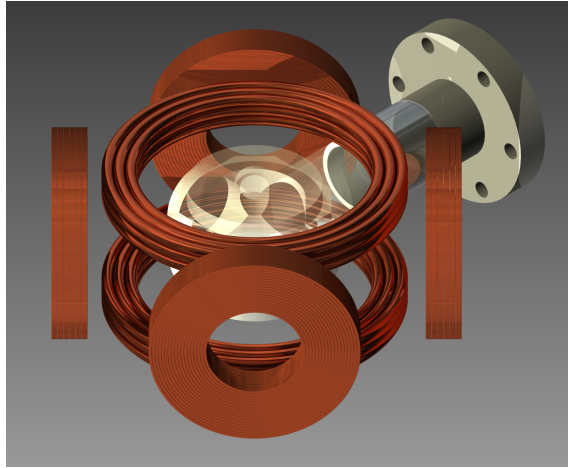


Figure 4: Sketch of the new setup. A coil pair in z-direction called z-coils. And two pairs of coil in x- and y-direction for tilting the magnetic field. Also the glass cell between the Coils is shown.

The old setup is built with coils in z-direction (z-coils) with magnetic fields up to  $600\text{ G}$ . The dipoles of these atoms could be polarized with small magnetic fields. The coils are used to orient all dipoles in z-direction for imaging (see chapter 6.2). Also coils in x- and y- direction (xy-coils) with 15 windings going up to  $1\text{ G}$  were created for compensation of the earth's magnetic field and other static fields [34]. Furthermore they were used for tilting the field to create the droplets and change their direction [35]. These coils are slow due to the large radius of the coils. Since we want to study droplets in any orientation with the  $7\text{ G}$  resonance, we have to

be able to apply magnetic fields up to 8 G in the xy-direction. Therefore we need additional coils.

A pair of coils in a Helmholtz configuration leads to a homogeneous field in first order [29]. The Helmholtz configuration has two coils with radius  $R$  whose distance is also  $R$ . The currents  $I$  in the two coils flow in the same direction and have the same magnitude. For a configuration with two single conductor loops, the magnetic field for  $z \ll R$  is [29]:

$$B(z) \approx \frac{\mu_0 I}{(5/4)^{3/2} R} \left[ 1 - \frac{144z^4}{125R^4} \right]. \quad (17)$$

In a large range ( $|z| < 0.3R$ ) between the two coils this approximation has less than one percent deviation [29]. The new setup of the coils is shown in figure 4 with the glass cell. The z-coils are in Helmholtz configuration.

Due to size constraints in the experiment the xy-coils cannot be built in Helmholtz configuration leading to a finite curvature of the magnetic field. This effect is measured in the following section (4.1).

A field gradient leads to a magnetic force  $F = -\mu_0\mu_m \nabla B$ . The force must be small and should not pull any atoms out of the trap. It can be used to levitate the atoms in the glass cell by compensating the gravitational field  $F_{grav} = mg$  with a gradient of 290.1 mG/mm for  $^{164}\text{Dy}$ . In the old setup of the experiment there are additional gravitation compensation coils [34] in anti-Helmholtz configuration. An anti-Helmholtz configuration is the same as the Helmholtz configuration but with currents in opposite directions. This leads to a constant gradient in z-direction. The new gradient coils have  $6 \times 12$  windings.

The magnetic field gradient of all other coil pairs is significantly lower and not important for magnetic fields smaller than 10 G.

## 4.1 Curvature and Strength of the Magnetic Field

In the previous section we explained the force due to the field gradient and the field stability for the tuning of the scattering length. This section is about the development of the coils. As a first step the possibilities to create magnetic fields which can be tilted in any direction are reviewed. Further constraints are low magnetic field curvature and therefore low off-center gradients, as characterized below. The magnetic field of a coil can be calculate with the Biot-Sarvart law [29]:

$$\mathbf{B}(\mathbf{r}_1) = \frac{\mu_0}{4\pi} \cdot I \cdot \int \frac{\hat{\mathbf{e}}_{12}(\mathbf{r}_2) \times d\mathbf{s}}{r_{12}^2}, \quad (18)$$

with the current  $I$  and the unit vector  $\hat{\mathbf{e}}_{12} = \frac{\mathbf{r}_{12}}{r_{12}}$ . This unit vector is the vector between the position of the current  $\mathbf{r}_2$  and the position  $\mathbf{r}_1$ .

After the Biot-Sarvart law a electrical current  $I$  leads to a magnetic field  $\mathbf{B}$ . However for a coil this integral is difficult to calculate. A useful approximation is to build the sum of the expression of the magnetic field of a single conductor loop over the number of loops in the coil. A simple analytic expression of a single conductor loop in cylindrical coordinates  $(r, \phi, z)$ , can be derived [36]. The radial part of the field is:

$$B_r = B_0 \frac{\gamma}{\pi\sqrt{Q}} \left[ E(k) \frac{1 + \alpha^2 + \beta^2}{Q - 4\alpha} - K(k) \right], \quad (19)$$

and the part of the magnetic field in z-direction is:

$$B_z = B_0 \frac{1}{\pi\sqrt{Q}} \left[ E(k) \frac{1 - \alpha^2 - \beta^2}{Q - 4\alpha} + K(k) \right], \quad (20)$$

with

$$\begin{aligned} B_0 &= \frac{\mu_0 I}{2a}, & \alpha &= \frac{r}{a} \\ \beta &= \frac{z}{a}, & \gamma &= \frac{z}{r}, \\ Q &= (1 + \alpha)^2 + \beta^2, & k &= 4 \frac{\alpha}{Q}, \end{aligned}$$

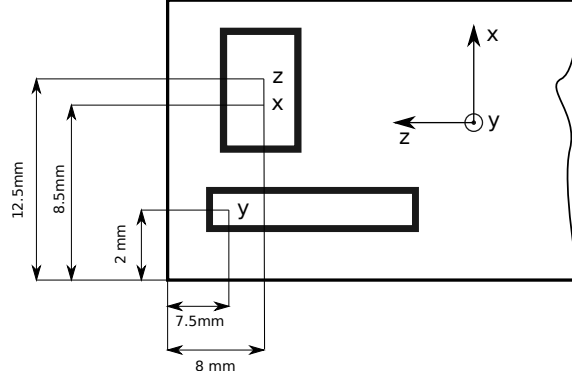


Figure 5: The sketch shows the magnetic field sensor [37]. The position of the sensors on the chip are not at the same place for all axis. This was measured with a razor blade.

and the Elliptical integrals:

$K(x)$  the complete elliptic integral of the first kind

$E(x)$  the complete elliptic integral of the second kind.

The center of the loop is the point of origin, therefore one also has to shift the center in the sum. Additionally the radius  $a$  of each winding is different. This leads to the resulting sums

$$B_z = \sum_N \left[ B_z\left(z - \frac{d(N)}{2}, a(N)\right) + B_z\left(z + \frac{d(N)}{2}, a(N)\right) \right], \quad (21)$$

$$B_r = \sum_N \left[ B_r\left(z - \frac{d(N)}{2}, a(N)\right) + B_r\left(z + \frac{d(N)}{2}, a(N)\right) \right], \quad (22)$$

with the radius of the winding  $a(N)$  and the distance between the coils  $d(N)$ .

Possible parameters of the coil setup are the number of windings, the distance between the loops, the radius of the loops and the current through the coils. But in our case the power supplies are limited to 4 A for the xy-coils and a current of 6 A for the z-coils. Therefore the z-coils are designed with  $3 \times 3$  windings (3 layers, with 3 windings each) for each coil with a radius and distance of 4 cm to obtain a

magnetic field of 1.55 G/A. They are made of wires with a square cross section of  $4 \times 4 \text{ mm}^2$  with a hole so that water cooling is possible and the coils can work at currents up to 600 G with the necessary power supplies.

The xy-coils have a diameter of about 6 cm and a distance between them of roughly 14 cm with  $6 \times 17$  windings. The coils are assembled using the "pancake" approach. One can wind two layers with higher precision compared to winding the six layers at once. After building three double-layer coils these are soldered and glued together to the final six layer coils.

The calculated field for these coils is 2.608 G/A with a curvature of the field in the coil axis direction of  $4 \text{ G/mm}^2\text{A}$  and in the other direction of  $2 \text{ G/mm}^2\text{A}$ . The wires have a rectangular cross section of  $1 \times 2 \text{ mm}^2$ . For coils that have been built with said dimensions, we have measured the magnetic field for various positions within the coils and a current of 1 A, see figures 6 and 7. The measured magnetic field is 2.3 G/A, which is 11 % lower than the calculated one. Yet, it is high enough to reach the 7.12 G resonance. The measured curvature of  $3.36 \text{ G/mm}^2$  and  $2.22 \text{ G/mm}^2$  for the x-coils and of  $3.90 \text{ G/mm}^2$  and  $1.84 \text{ G/mm}^2$  for the y-coils are also near the calculated ones (see table 1). The strength of the earth's magnetic field is in the same range. Every point was first measured with the power supplies off (although there are small leak currents of  $\sim 15 \text{ mA}$ ) as reference. Then we applied a set current of 1 A at the power supply and measured the magnetic field for different positions on the symmetry axis as well as perpendicular to it. The results are shown in figure 6.

Both coil pairs should have the saddle of the magnetic field between the coils so that the position with the lowest gradient of the field coincides spatially for all coil pairs. In the measurement however there was a small offset, as can be seen when taking a look at figures 6a, 6c, 6e and comparing them with figures 6b, 6d, 6f. The saddle should be at the same position but there is a difference between 2 and 7 mm. This offset can be explained easily. The used magnetic field sensor is built in the institute [37] and one has to note that the sensor consists of 3 separate sensors for each magnetic field axis, mounted on a chip. These three sensors are at slightly different places on the chip. With a razor blade the positions of the sensors were measured, also shown in figure 5. The difference in the measurements of magnetic field of the coils match the effect of the offset position within a  $\pm 1 \text{ mm}$  error.

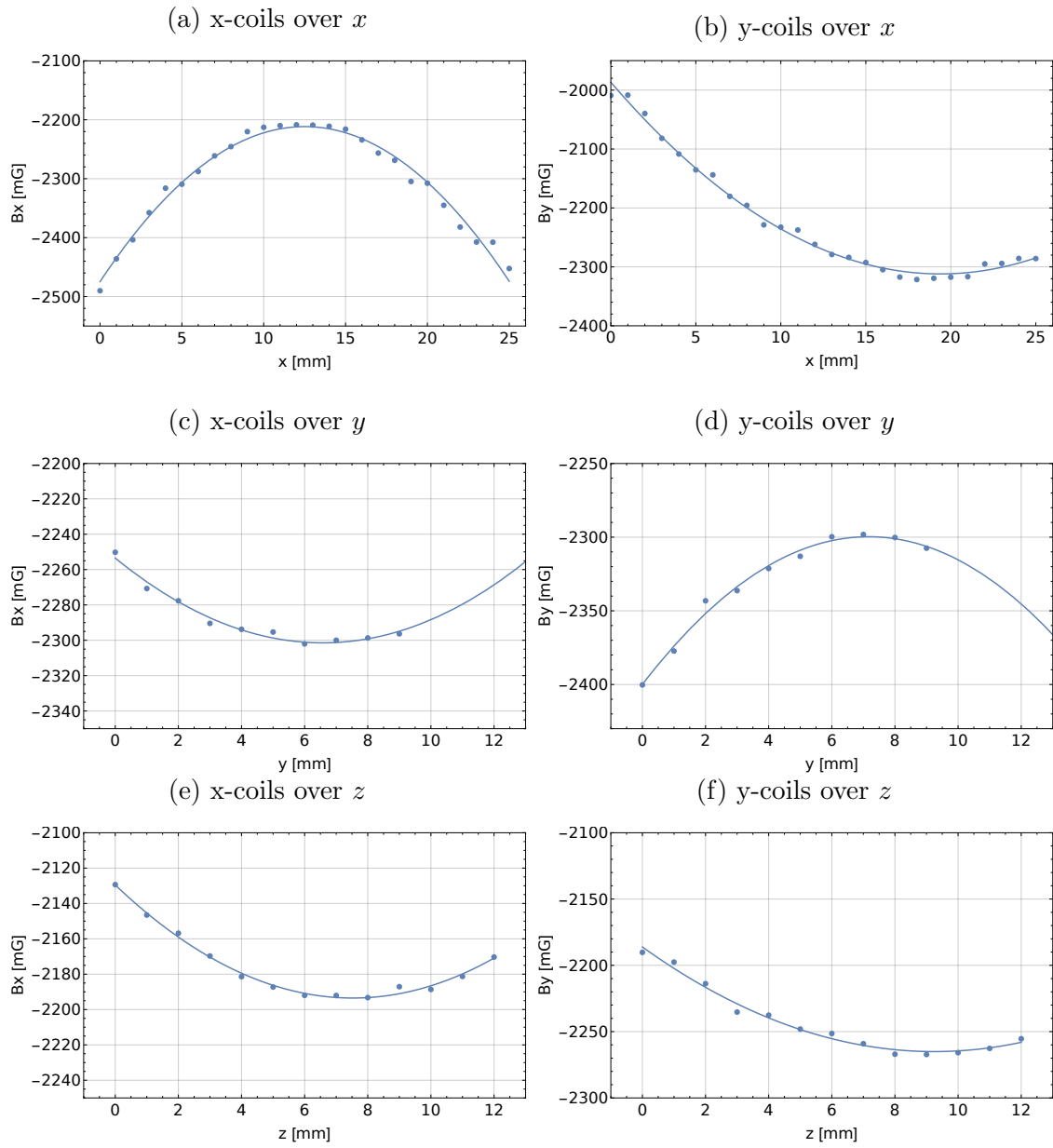


Figure 6: The magnetic field of the xy-coil pairs over the position at 1 A. The magnetic fields are not constant over space as expected. Fitted values for magnetic field and curvature are summarized in table 1.

The used power supplies are HighFinesse Bipolar-Current-Source (BCS) supplies

Name	Windings	Impedance [ $\mu\text{H}$ ]	Resistance [ $\text{m}\Omega$ ]	Curvature [ $\text{mG}/\text{mm}^2\text{A}$ ]	Strength [ $\text{mG}/\text{A}$ ]
z-coils	$3 \times 3$	29	130	0.0927	1552
x-coils	$17 \times 6$	1110	590	$x : 3.36$ $y, z : 2.24$	2235
y-coils	$17 \times 6$	1130	550	$x : 3.90$ $x, z : 1.79$	2291
Grad Coils	$12 \times 6$	586	830		

Table 1: Data of the different new coils. The magnetic field of the gradient coils was not measured because there was not enough space in the PVC cage with the coils inside.

rated up to 4 A and 5 V. The supplies have a high precision of  $\delta I < 1 \times 10^{-4}$  A, are fast depending on the impedance and were built to control the current in experiments. To use a 3 mG wide Feshbach resonance a current precision of at least 1 mA is needed.

The coils are mounted in a milled cage of PVC. The plastic PVC can be used up to a temperature of 80 °C. To get a magnetic field up to 600 G the z-coils are water cooled so a current of 350 A does not heat the coils above the temperature limit of PVC. Although a current of 10 A would heat the uncooled xy-coils above 100 °C.

In the cooling sequence, when the thermal cloud is cooled down to the BEC phase, only the z-coils are planned to be used. For higher temperatures the size of the thermal cloud (with tens of  $\mu\text{m}$ ) of the dysprosium atoms is much larger than in an ultra-cold BEC (with few  $\mu\text{m}$ ). In the latter case Feshbach resonances play a more important role, yet the higher gradient of the xy-coils is not important.

## 4.2 Impedance and LCR Circuits

Technically it is possible to tune the dipolar interaction with the new coils. Therefore higher frequencies than the trap-frequencies are needed (see chapter 6.2). For the previous chromium experiment fast magnetic field rotations were not achievable, because eddy currents were induced in the steel chamber [28]. The new coils are designed around a glass cell, where this problem is circumvented. In the following we investigate the achievable switching times of the new coils.

For rotating the magnetic field or switching the coils on and off, the electrical

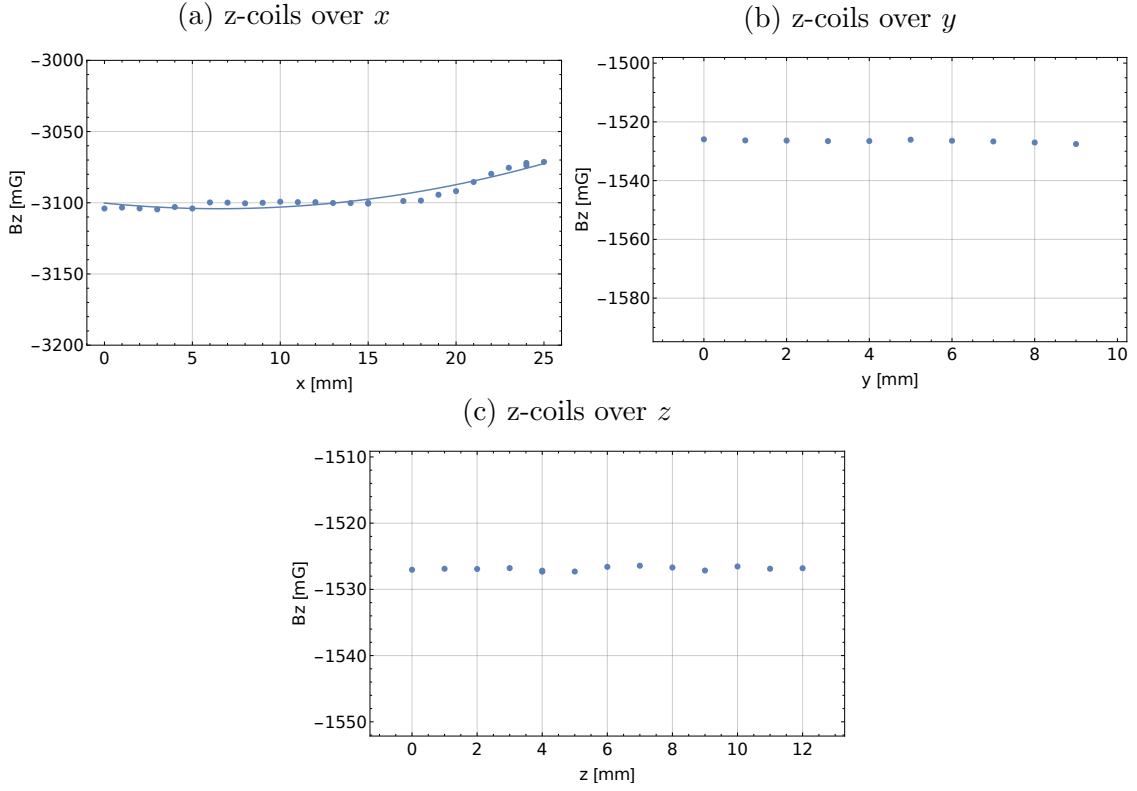


Figure 7: The magnetic field over the position at 2 A for the first and 1 A for the last two plots. The field of the z-coils is nearly homogeneous. Fitted values for magnetic field and curvature are displayed in table 1.

reactance  $X$  or impedance  $Z = R + iX$  are important. One can think about building coils with many windings to make high magnetic fields possible, however this would increase the switching time. To get a small impedance  $L$  the coils should not have too many windings, since  $L \propto N^2 A$  [29]. This is why the z-coils with 9 windings are much faster than the gradient coils (72 windings) or the xy coils (102 windings).

The coils need time to build up the magnetic field. Consequently the current has a delay to the applied voltage  $U = L\dot{I}$ . When driving the coils at low frequencies  $\omega \ll \omega_{cutoff}$  the electrical reactance  $X$  vanishes proportionally to the frequency and the inductance  $L$ ,  $X_L = \omega L$ . To receive the cutoff frequency one can calculate the parameters of the LR-circuit. The sum over the voltage of the coil  $U_L$  and the resistor  $U_R$  has to be zero in the non-driven state. To solve the differential equation

$$\begin{aligned}
U_L + U_R &= 0 \\
L \frac{d}{dt} I + RI &= 0 \\
Li\omega I + RI &= 0 \\
\omega &= iR/L
\end{aligned} \tag{23}$$

an alternating current  $I = I_0 \exp^{i\omega t}$  can be used. The cutoff frequency is  $\omega_{cutoff} = R/L$  and the time constant is  $\tau = L/R$ . An imaginary frequency corresponds to an exponential response  $\propto e^{-i\tau}$  of the current (and thus the magnetic field) after a voltage step.

The z-coils have a very low inductance of around 10  $\mu\text{H}$  and a resistance of 130  $\text{m}\Omega$ . Thus the cutoff frequency is 8 kHz corresponding to a switching time of 0.13 ms.

The xy-coils have a higher resistance (590  $\text{m}\Omega$ ) and a higher inductance of about 540  $\mu\text{H}$  and therefore a cutoff frequency of 147 Hz therefore switching time of 6.7 ms. But this is only valid for voltage controlled power supplies. In all setups the power supplies are actively current-controlled. Therefore the switching times are typically faster. In a voltage controlled system a higher resistance leads to a higher cutoff frequency. At frequencies larger than the cutoff frequency the reactance will be higher than the resistance. This is not the case in a current controlled system.

The current-controlled power supplies regulate the voltage, that a higher voltage is applied on the coils in the beginning. With this the magnetic field is reached faster.

In figure 8 the frequency dependency of the z-coils is shown, due to some noise an additional high power resistor with 1  $\Omega$  is used. There is a difference between the current obtained from a sinus fit and the peak to peak value. This means there are some higher frequencies above 1 kHz, but the main value of the current is constant till 3 kHz. The cutoff frequency of the z-coils is at 12 kHz.

The frequency dependency of the xy-coils is shown in figure 9. The cutoff frequency of the two coil pairs is slightly different. A possible reason for this could be the aluminum plate on which the coils are mounted. Eddy currents appear at high frequencies in the aluminum plate. Although in steady state the aluminum is

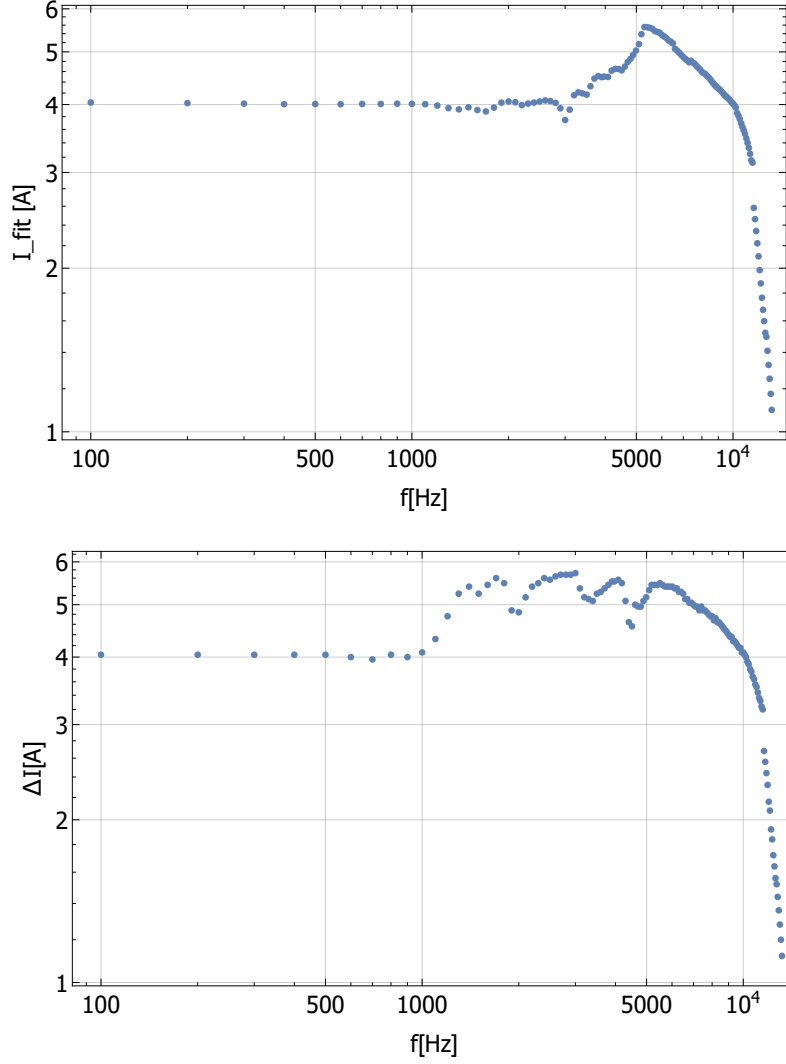


Figure 8: Bode plots for the z-coils of fitted current (top) and peak-to-peak current (bottom). Compared to the expected low-pass behavior, the current-controlled power supplies induce larger currents for high frequencies. This way the cutoff frequency is 12 kHz.

not magnetic. For static magnetic fields  $\mu_r$  of aluminium is 1. So the resonance frequency shifts if a plate is next to the coils. In the experimental setup the vacuum parts made of steel should also be considered.

For the z-coils the cutoff frequency is high enough but for the xy-coils it is too low as we want to tune the DDI with rotating magnetic fields. But for the tuning of

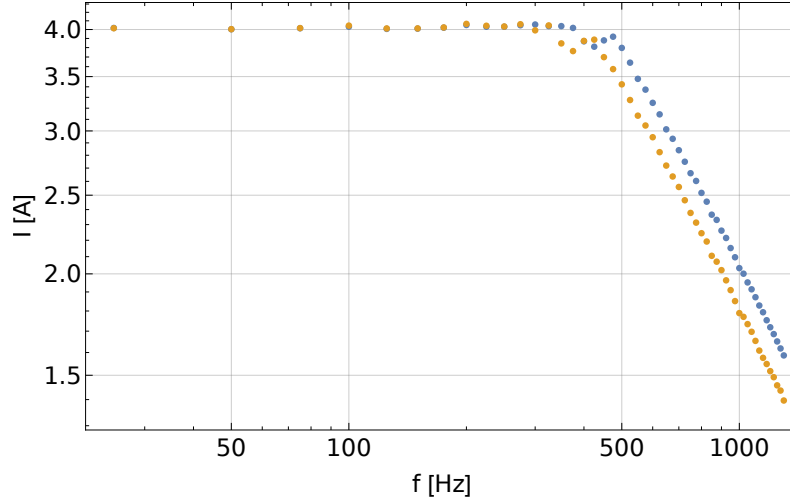


Figure 9: Bode plots of the x- (blue) and y- (orange) coils. Here the cutoff frequency is much lower at 500 Hz because of the higher numbers of windings compared to the z-coils.

the DDI only a single frequency is needed. This makes a resonant circuit possible. On resonance the reactance  $X$  should vanish (thus  $Z = R$ ) to reach the desired currents, which can be achieved with a serial LCR circuit. In contrast, for a parallel circuit the reactance is maximal on resonance. The impedance of a serial LCR-circuit is

$$Z = R + i \left( \omega L - \frac{1}{\omega C} \right). \quad (24)$$

The resonance frequency can be calculated like the cutoff frequency in formula 23. The sum over all voltages should be zero. But now with an additional capacitor term  $U_C = 1/c \int I dt$  this equation changes to

$$\omega^2 I - \frac{1}{CL} I + i \frac{R}{L} \omega I = 0. \quad (25)$$

The resonance frequency is then given by

$$\omega_0 = i \frac{R}{2L} \pm \sqrt{\frac{1}{LC} - \frac{R^2}{4L^2}}. \quad (26)$$

For the coils considered in this thesis the damping  $\delta = R/2L$  can be neglected. With a capacity of  $1 \mu\text{F}$  and an inductivity of  $2 \cdot 540 \mu\text{H}$  the resonance frequency

of a coil pair should be at  $f_0 = 5 \text{ kHz}$ . The electrical reactance at the resonance frequency is zero so in a serial case the impedance is minimal. But the voltage drop at the capacitor is much higher than the voltage from the power supply due to the resonance:

$$\begin{aligned}
 CU &= Q \\
 I &= \dot{Q} = C\dot{U} \\
 U_0 &= \frac{I_0}{C\omega_0} = \frac{4\text{A}}{2\pi \cdot 5 \text{ kHz} \cdot 1 \mu\text{F}} \approx 127 \text{ V}.
 \end{aligned}
 \tag{27}$$

This leads to an effective voltage of 90 V that is at the maximum ac voltage rating of 90  $V_{ac}$  for the 1  $\mu\text{F}$  KEMET R75 capacitors, the 220 nF capacitors work with higher voltage. This voltage was also measured with a multi-meter.

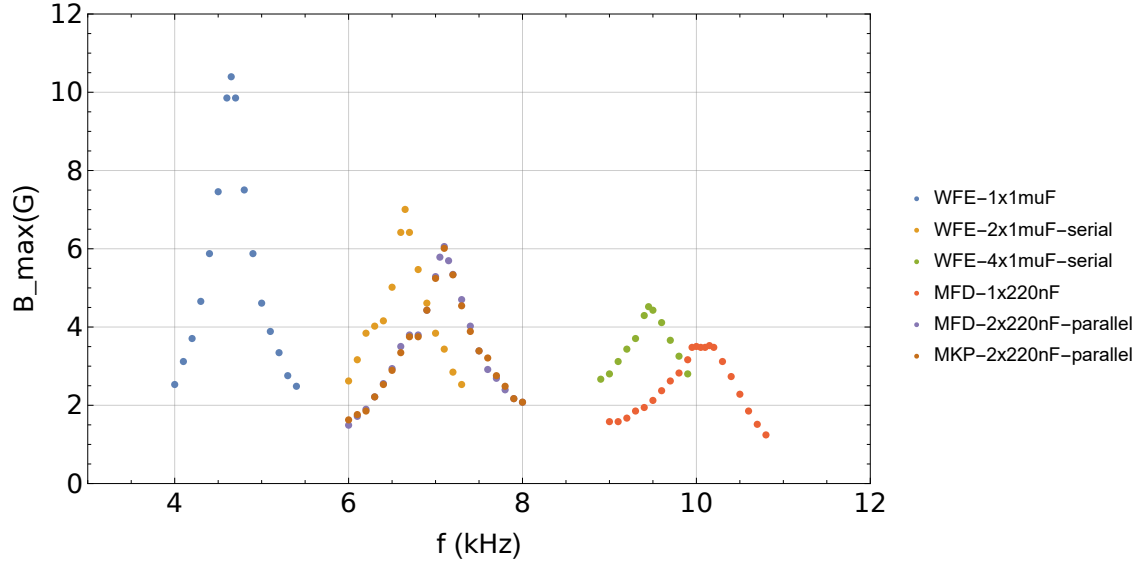


Figure 10: Maximum magnetic field over frequency for several LCR circuits consisting of the x-coils and different capacitor combinations. In theory the maximum amplitude is independent of frequency. Yet with the current-controlled power supplies we observe a strong frequency dependence. Since we need 4 A in the setup only a frequency of 5 kHz is suitable.

In figure 10 the resonances for different capacitors in series with the x-coils are shown. The names and the capacity of the used capacitors are given in table 2.

Name	Capacity	V-Range [ $V_{ac}$ ]
KEMET R75	1 $\mu$ F	90
KEMET R75 (MKP)	0.22 $\mu$ F	250
EPCOS B32686	33 nF	550
Panasonic ECWFE (WFE),	1 $\mu$ F	170
Cornell-Dubilier 940C (MFD),	220 nF	500

Table 2: The capacities of all used capacitors.

Although only the resistance of the coils should be important at the resonance of a LCR circuit there is a strong frequency dependency. A LCR circuit with a resonance at higher frequency leads to less peak-output. This behavior is independent of the capacitor model and manufacturer. The necessary current to use the Feshbach resonance at 7.1 G limits the driving frequency to a value of  $\sim 5$  kHz. This is well above the trap frequencies and higher than typical internal energies of the quantum gas (see chapter 6.2). An additional 33 nF capacitor for the x-coils is used to match the resonance frequency of the y-coils, see figure 11. For the z-coils there no LCR circuit is needed, since the power supplies are able to drive them up to  $\omega_{cutoff} = 12$  kHz.

Since one needs bipolar capacitors for AC circuits, the electrolytic capacitor does not work. Therefore film capacitors with polypropylene as dielectric medium are used. Such capacitors can work with high ac voltage (90 V) and high frequencies up to 1 MHz.

In a LCR circuit it is not possible to get an additional static magnetic field, so for compensation of static fields the coils of the current setup are needed as well. For the rotation of the dipoles it is important that not only the resonance frequency of both coil pairs is the same, but also the amplitude of the magnetic fields can be matched. To rotate the magnetic fields the two LCR circuits for x- and y-coils need to be driven out of phase. For this purpose two SRS DS345 function generators with interconnected timebase were used to realize a fixed phase relation.

After turning the devices on, the fixed relative phase is randomly set. Therefore one has to measure the phase and shift it to  $90^\circ$ . The output of the generators can be tuned in steps of 0.01 V up to 10 V. But the current through the coils is not linearly dependent on the input power in the LCR circuit case. Hence one had

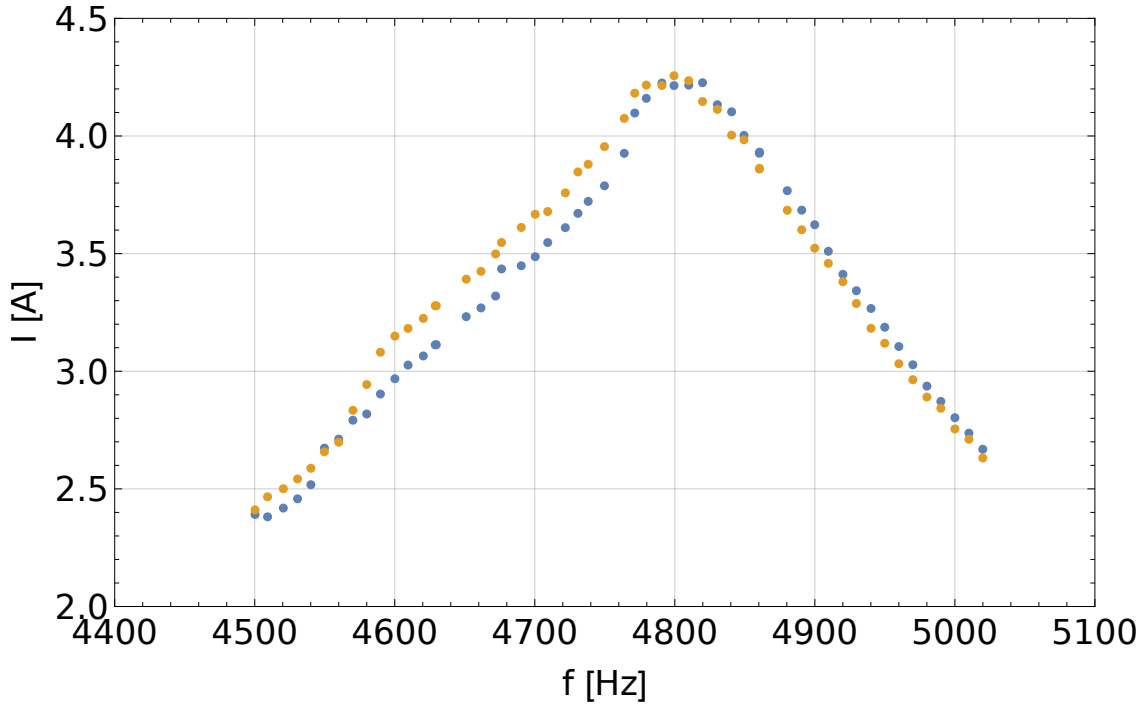


Figure 11: The x as well as the y coil pair should work at the same frequency, in this case the y-coils(orange) have the capacitor MKP-1  $\mu\text{F}$  and the x-coils (blue line) an additional 33 nF capacitor

to measure the current and actively control the power to get the desired magnetic field. As we have shown in this chapter, the coil pairs have low enough gradients of the magnetic field at 8 G. Therefore we can use the Feshbach resonance. Also LCR circuit make high rotation frequencies of the magnetic field possible. This can be used to tune the DDI.

## 5 Magnetic Shielding

To get a BEC with high atom number it is important to control the scattering length with high precision. The Feshbach resonances we use for tuning this length are only a few mG wide, therefore we need a precise magnetic field.

At a low magnetic field the dysprosium atoms are not polarized any more and can have magnetic spin exchange collisions. Thus the atoms can interact with their neighbor via the DDI in a lattice [38, 39]. Therefore again low magnetic fields in the range of mG are required.

In the current experimental setup it is possible to compensate stray magnetic fields with the coils mentioned in the previous chapter down to the mG level. To see the mentioned effects, it is necessary to compensate the magnetic fields even further, so we plan to add a passive shielding with a mu-metal box to the active compensation with the coils.

Mu-metal is an alloy of nickel and iron and has a high permeability of over  $\mu_r = 100\,000$  for low magnetic fields. In these materials the magnetic flux density is highly increased. Thus they can be seen as "conductors" for magnetic field lines. To shield a device from surrounding magnetic fields it can be covered in mu-metal, as shown in figure 12 for a ring geometry.

In the booklet of the company Sekels [40] simulations of magnetic shielding are given, shown in figure 13, where red color indicates a higher magnetic field than the blue color. Figure 13a shows the source of the field without any shielding material. Figure 13b shows the effect of a 1 mm thick material with a permeability of  $\mu = 500$ . The shielding effect of this material is very small. But also the effect of a single plate made of a 1 mm thick mu-metal with a permeability of  $\mu = 50\,000$  is small. Only next to the plate there is a mentionable shielding effect. The best shielding is achieved with a closed box (figure 13d).

For the first test of a passive magnetic shielding we used a film of mu-metal with a thickness of 0.1 mm. To create a magnetic field the coils built for compensating the gravitation and for rotating the magnetic field, described in chapter (4.1), were used.

The parameter to describe the effect of the shielding is the shielding ratio. Therefore the magnetic field with and without a shielding parameter was measured (see

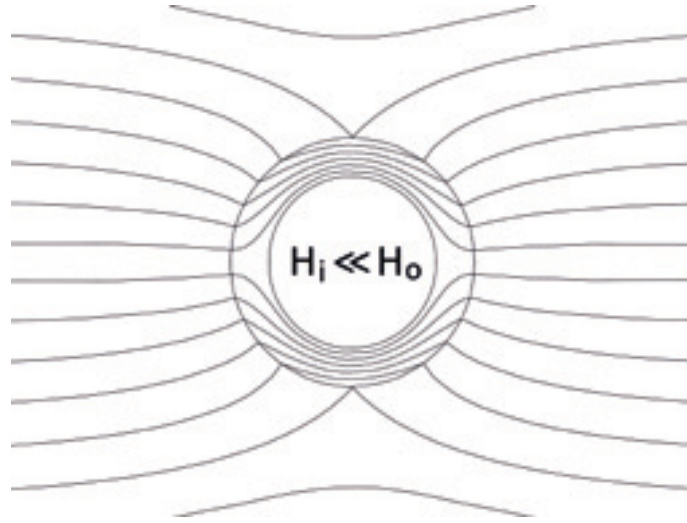


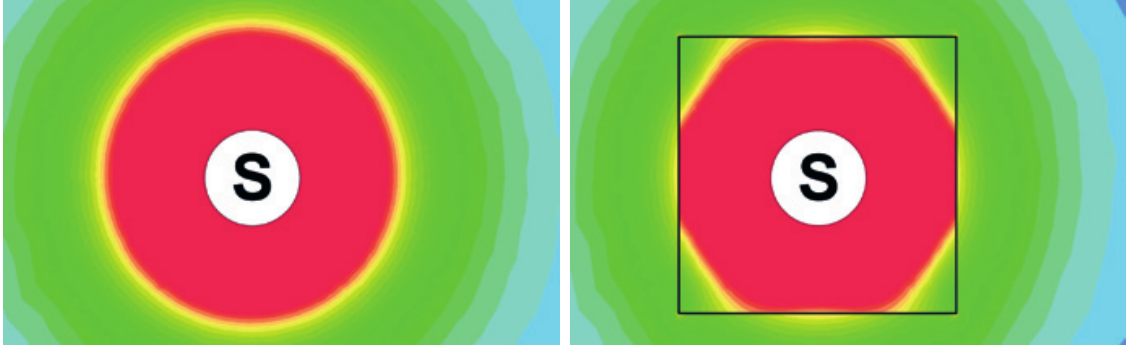
Figure 12: A ring of mu-metal in a homogeneous magnetic field. The strength of magnetic field  $H_0$  outside of the ring is much larger than inside  $H_i$ , because the magnetic field is bent in the ring. Figure taken from [40].

inset of figure 14). For the measurement the coils were 2 cm away from the mu-metal film, which corresponds to  $x = 0$  in figure 14, leading to a magnetic field of about 2 G at the sensor without shielding.

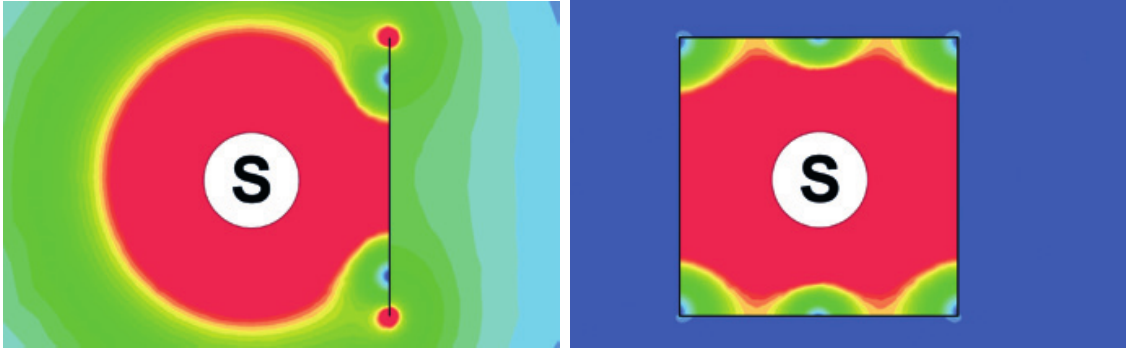
In figure 14 the shielding ratio for 0.1 mm thick films with different plate sizes is shown. The plates are plate1 with 28 cm  $\times$  19 cm, plate2 with 13 cm  $\times$  13.5 cm and plate3 with 9 cm  $\times$  8.5 cm. Larger plate sizes have larger shielding ratios. Figure 13 also makes clear, that a single layer in one direction is not enough to efficiently shield the magnetic field. Because of this we decided to build a box to test the shielding. The box, as depicted in figure 14, has the highest shielding ratio, a length of 28 cm, a width of 17 cm and a height of 23 cm.

By comparison to the box adding a second layer of the 0.1 mm thick mu-metal plate, giving effectively a 0.2 mm thick plate, has a smaller shielding effect. In figure 14 it can be seen that the shielding ratio is higher next to the film than in the center of the box. With space between the layers, this shielding ratio could be higher, which might have to be taken into account during the creation of the shielding for the next setup.

In the following, the measured values are compared to the theory. To do this



(a) A source  $S$  of a magnetic field without shielding. (b) A box (width= 5 m, thickness=1 mm) made of a material with  $\mu = 500$ . No mentionable shielding of the magnetic field is achieved.



(c) A plate made of a material with  $\mu = 50\,000$ . Meters away there is again no significant effect. (d) A box made of a material with  $\mu = 50\,000$ . Outside of the box there is only a small magnetic field left. The magnetic field inside however is changed dramatically.

Figure 13: Simulations of a material with a permeability of 500 and a mu-metal placed inside a magnetic field. The effect of magnetic shielding is shown in the color code, red are high magnetic fields and blue are low fields. Figure taken from [40].

it is important to know, that the calculation of the shielding ratio depends on the geometry used. For the calculation of the shield ratio of a sphere the [40] following formula [40]

$$S = \frac{4}{3}\mu_r d/D + 1 \quad (28)$$

is given, with  $S$  the shield ratio,  $\mu_r$  the permeability of the mu-metal film,  $d$  the

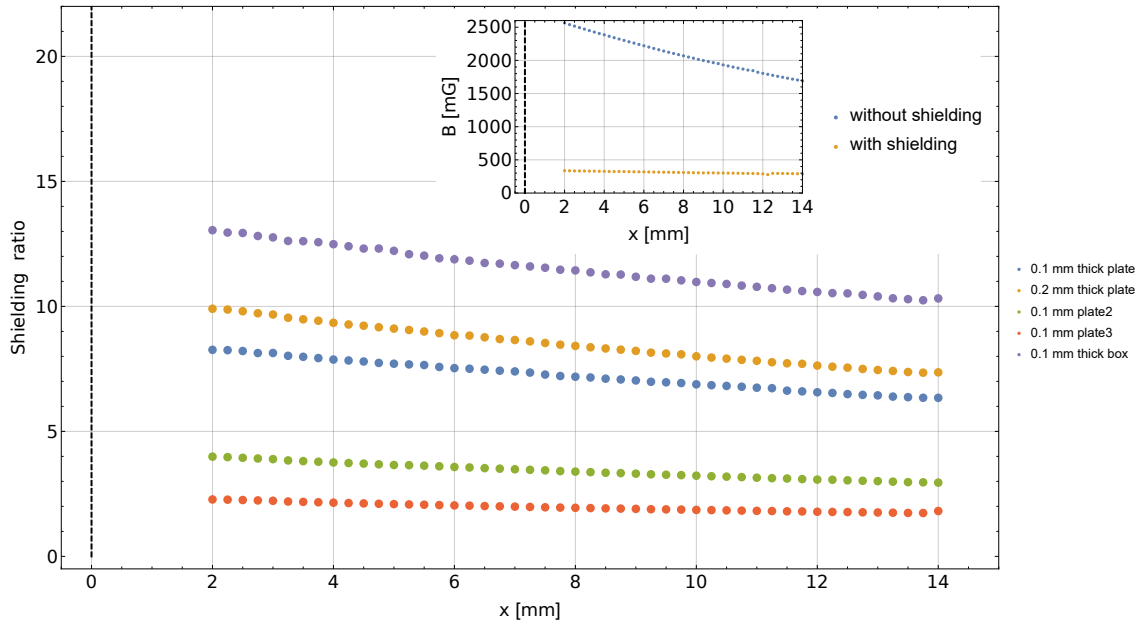


Figure 14: Comparison between different layers of mu-metal. The magnetic field is applied by a coil of the xy-coil pairs but not shown by the plot at position  $x = -20$  mm. The mu-metal film located at  $x = 0$  (black line). The inset shows a magnetic field measured with and without shielding. The ratio between them gives the shielding ratio. With increasing size of a plate, the shielding ratio increases. Adding a second layer increases the shielding however using a complete box is more useful and efficient in practice.

thickness of the film and  $D$  the diameter of the sphere.

The box we built is  $28 \times 17 \times 23$  and in the booklet from the company Sekels, they mention that a cuboid can be approximated as a sphere with the space diagonal as the diameter

$$S = \frac{4}{3} \mu_r d / \sqrt{a^2 + b^2 + c^2} + 1. \quad (29)$$

Thus the shielding ratio of our box with a permeability of around  $\mu_r = 100\,000$  would be  $S = 36.2$ . In our measurement we have a shielding ratio of around  $S \approx 9$  the permeability that would lead to this is  $\mu_r = 20\,000$ .

For an experiment a fully closed box is not possible, because one needs holes for lasers, a vacuum chamber, or even wires for controls and sensors. The holes lower the efficiency of such shielding.

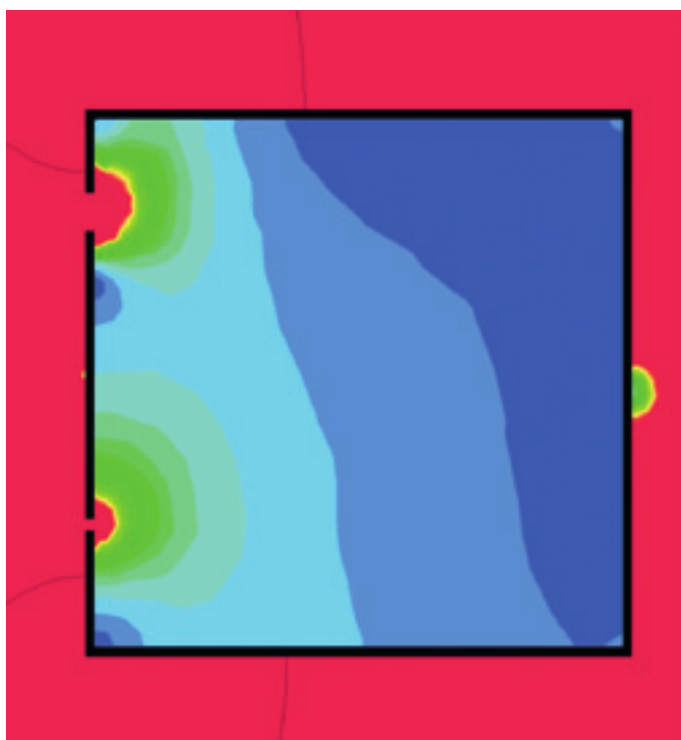


Figure 15: Simulation of a mu-metal box placed inside an homogeneous magnetic field. The effect of holes in the box can clearly be seen in comparison to figure 13d. In figure 13d, the source of the magnetic field, was inside the mu-metal box, here the source is outside and the magnetic field leaks into the box. Figure taken from [40].

In figure 15 the influence holes in a box made of mu-metal have, on the magnetic field shielding are shown. The source of the magnetic field is not shown, it is to the left outside of the mu-metal box. In figure 16 our own measurements with holes are shown. Few centimeters away from small holes the effect of such holes seems feasible for the experiment. Hole1 and hole2 have a diameter of 4 mm. The measurement of hole2 is off-centered by 2 cm. With all other holes the sensor is centered to the hole. Hole3 is a 10 mm hole and hole4 has a diameter of 15 mm. A significant effect was only noticeable in immediate surroundings of the holes.

We use coils in the Helmholtz configuration to tune the contact interaction with the Feshbach resonance. Because of this we look at the effect of the mu-metal on the shape of the magnetic field. Therefore a coil pair in Helmholtz configuration has not a constant magnetic field anymore as one can see in figure 17. Hence one wants

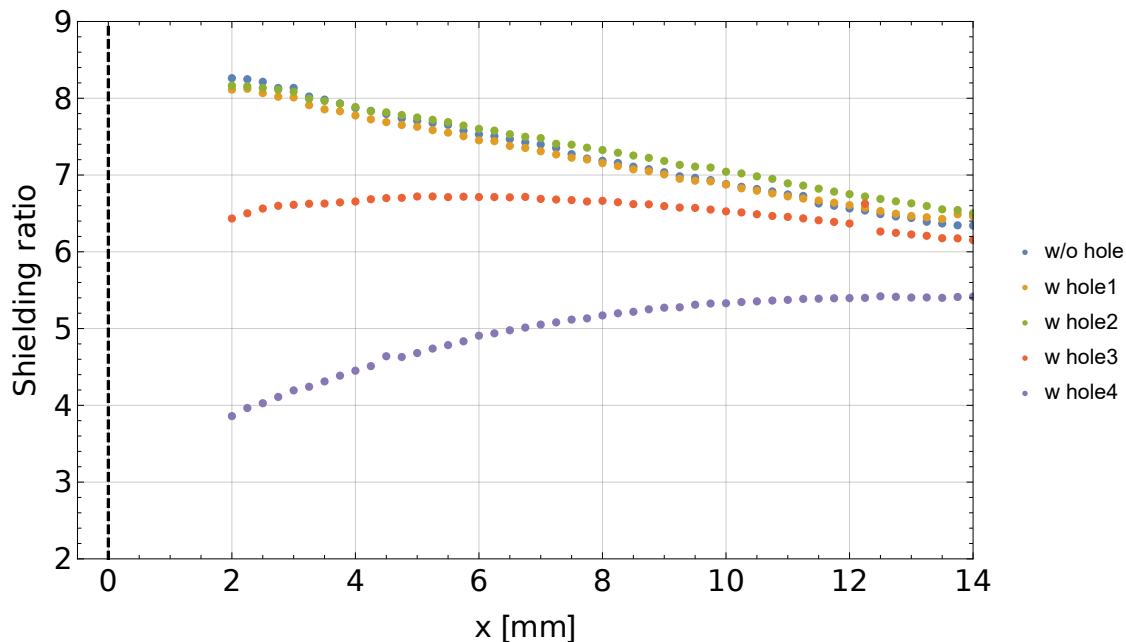


Figure 16: Influence of different sized holes in the mu-metal film on the shielding ratio of a single 0.1 mm thick film.

to have coils in the chamber for something like Feshbach resonances or tilting the field, the box must be much bigger than for only shielding. Another solution is to wind the wires around the eight walls of the box. There are mirrored currents in the mu-metal so the magnetic field inside is very homogeneous. This leads to a higher impedance and therefore to long switching times. These longer switching times are not feasible for the experiment. Therefore the measured disturbance of what should be a homogeneous field inside a pair of coils in Helmholtz configuration due to the mu-metal has to be taken into account in the planning of a magnetic shielding for a new experimental setup.

In figure 18 the permeability of mu-metal  $\mu_r$  is shown over the magnetic field  $H$ . It is evident that there is a huge difference between annealed mu-metal and cold-formed mu-metal. The film of mu-metal we used was annealed. But with bending the film to the box or cutting the film into the plates, the magnetic properties change dramatically and the permeability decreases. Therefore for a effective shielding, it is necessary to anneal the mu-metal box in the final form to keep all magnetic properties. So far we haven not distinguished between the magnetic flux density

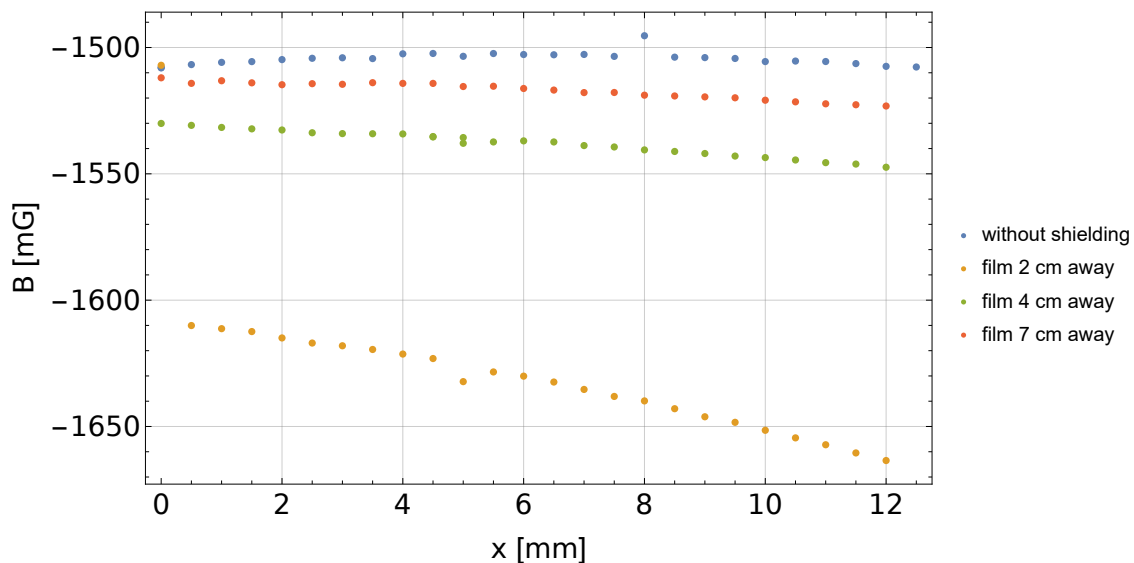


Figure 17: Influence of a mu-metal film close to a pair of coils in Helmholtz configuration. Without the mu-metal the field is homogeneous with a constant amplitude. With the mu-metal close by, the magnetic field is clearly disturbed.

$B$  [G] and the magnetic field  $H$  [A/m]. The magnetic flux density depends on the material, while the magnetic field  $H$  is independent. The permeability of the mu-metal film is dependent on the magnetic field, like most other materials. In a material the magnetic field is given as

$$B[T] = \mu_r \mu_0 \cdot H[A/m]. \quad (30)$$

In the mu-metal the magnetic flux density is much higher than in the vacuum. A magnetic field amplitude of 12 mG in a vacuum corresponds to a magnetic field of 1 A/m. Therefore the maximum of the permeability of annealed mu-metal, given by the booklet of Sekels [40] is at around 24 mG, as shown in figure 18.

In figure 19 the shielding ratio over magnetic flux density is shown. There is a maximum at around 8 G for the box as well as for the plate. At this value the magnetic field inside the mu-metal should be saturated and the permeability should only decrease. According to formula 29 a shielding ratio of 20 corresponds to  $\mu_r \approx 20000$  for the given box dimensions. In contrast the expected permeability is

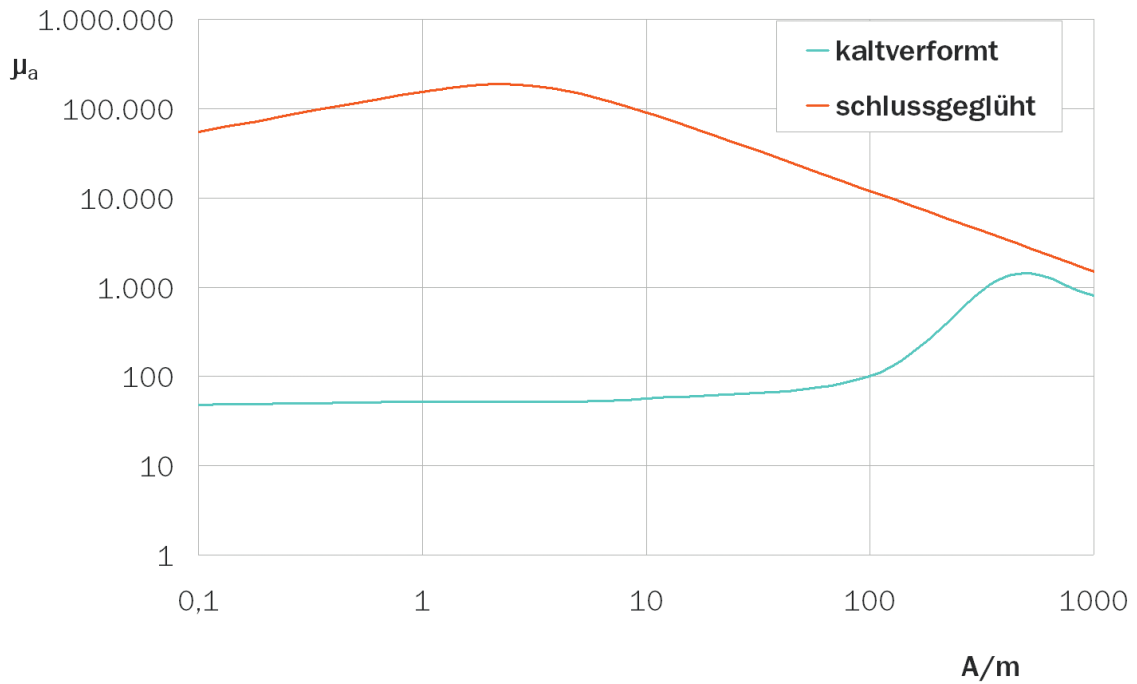


Figure 18: The permeability of mu-metal depending on the magnetic field  $\mathbf{H}$ . The red line is hot annealed ("schlussgeglüht") metal and blue curve is cold formed("kaltverformt") metal. Figure taken from [40].

on the order of 2000 at 8 G ( $\hat{=}600$  A/m), as depicted figure 18. This mismatch could be due to some geometry effects, or inhomogenities of the magnetic field. In order to plan such a box with the necessary optical access for the experiment it is crucial to carry out numerical calculations as presented in figure 13. Only this way, field inhomogenities can be taken into account and feasible predictions of the shielding ratio are possible.

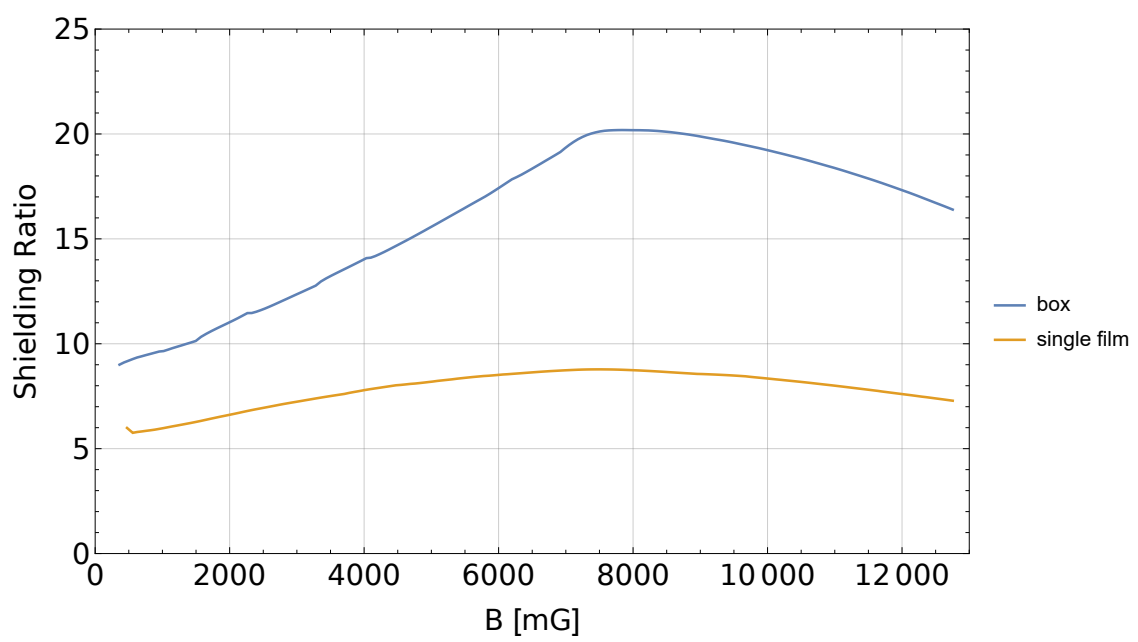


Figure 19: The shielding ratio over the applied magnetic field.

## 6 Rotating Quantum Droplets

In this chapter the behavior of quantum droplets within a rotating magnetic field is explained. First the rare earth element dysprosium is described. The next section explains the setup of the experiment with the optical-dipole-traps and therefore the laser beams as well as the *in situ* imaging. Then, in the next section regarding on the rotating droplets are shown.

### 6.1 Dysprosium

Solid dysprosium is a rare earth metal and a lanthanide. Because of its 66 electrons, dysprosium is far away from the theoretical description of a hydrogen-like atom. Using Hund's rules we get an  $^5I_8$ -state as the electronic ground state. There are many optical transitions accessible by visible light starting from this ground state, some of which can be used for laser cooling.

Dysprosium has seven different stable isotopes. This is important, because the total spin consists of the electron spin and the nucleon spin. It determines whether the atom acts like a fermion or a boson. The isotopes with the highest natural abundance are the bosonic  $^{164}\text{Dy}$  (28.3%) and  $^{162}\text{Dy}$  (25.5%) and the fermionic isotopes  $^{163}\text{Dy}$  (24.9%) and  $^{161}\text{Dy}$  (18.9%). The bosons do not possess a nuclear spin and thus no hyperfine structure. Our group mainly works with the bosonic  $^{164}\text{Dy}$ . The scattering length of dysprosium is not well known. Measurements with thermal atoms [41, 42] give  $a_s = 92(8)a_0$  for the background scattering length of  $^{164}\text{Dy}$ . However, results on the critical atom number [12] and collective oscillations [43] indicate  $a_s \approx 70a_0$ . The ratio of the strength of the DDI compared to the CI in dysprosium, far away from any Feshbach resonance, is given by  $\epsilon_{dd} \approx 1.4$  for  $a_s = 92$  (or  $\epsilon_{dd} \approx 1.9$  for  $a_s = 70$ ).

### 6.2 Experimental Setup

As the first step an oven heats dysprosium up to 1200 °C, which is below its melting point of 1412 °C, to evaporate some atoms into the gas phase. The hot atoms then need to be cooled down. The first step is executed with transverse laser cooling followed by a Zeeman slower. After that the atoms can be trapped in a magneto

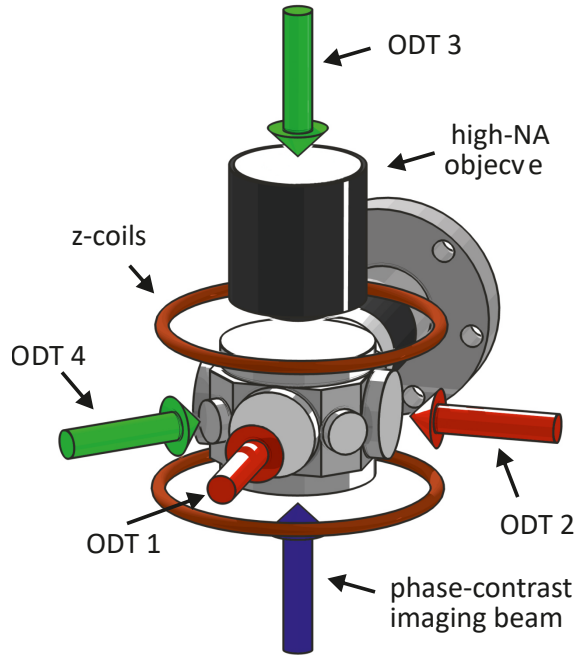


Figure 20: Schematic view of the experimental setup consisting of the the glass cell and the used laser beams. Adapted from [34].

optical trap (MOT) [44]. Then the atoms of the MOT are loaded into an optical dipole trap (ODT).

With this approach atoms are trapped inside a laser beam due to the force of the light on them. The electric field of the light induces an electric dipole moment  $\mathbf{p} = \alpha\mathbf{E}$ . This induced dipole experiences a force  $\mathbf{F} = \nabla(\mathbf{p} \cdot \mathbf{E})$ . Thus the atoms experience a force pointing either to high intensities of the laser beam (which can then be used as a trap) or to lower intensities depending on the sign of polarizability  $\alpha$ . The former can be achieved by a red-detuned light field. In the next step we transport the atom cloud into a single ODT at a wavelength of 1070 nm to the glass cell, because of better optical access and better access with the coils (see figure 20). In the glass cell we use several beams with different wavelengths to trap the atoms. After the transport the atoms are loaded into the crossed ODT. The crossed dipole traps (ODT1 & ODT2) work at a wavelength of 1064 nm. The lasers used for the traps have a nearly Gaussian spatial intensity distribution and in the cold regime the atoms are close to the minimum of the potential. Therefore the potential can

be approximated as a harmonic oscillator, where the trap frequencies are given by the curvature of the potential at the minimum [34]. A magnetic field oscillating with the trap frequency can excite shape oscillations in dipolar gases for example the quadruple mode [45].

From the top an additional laser beam (ODT3) at a wavelength of 532 nm with an electro-optical deflector system (EOD) is aligned onto the atom cloud. With an EOD it is possible to move a laser beam by using the Pockels effect. The tilt angle of the beam is then directly dependent on the applied voltage [46, 47]. Since this can be done very fast the atoms do not experience a single laser beam at different positions but rather a time averaged potential.

The last optical dipole trap (ODT4) is a so called "light sheet" with a wavelength of 532 nm. Along one axis the laser beam is expanded with cylindrical lenses or with a pair of tilted prisms, so that in the focal point one direction is much smaller than the other. This leads to a narrow confinement of the BEC in one direction. In the described traps we can then reach a BEC by evaporative cooling and then conduct our experiments.

To make the atomic cloud visible we then need to image it. We are not only able to take time of flight (TOF) pictures but also *in situ* pictures. Without TOF, in which the atom cloud expands, the atom cloud is much smaller and thus a high-resolution objective is needed [11]. Likewise also the atom density of the cloud is much higher therefore absorption imaging is not useful because the pictures would then be saturated. Instead we use phase contrast imaging. A linear polarized blue laser detuned by several linewidths with respect to the transition at 421 nm is used and since our laser points in the direction of the magnetic field, this means it is a combination of  $\sigma^+$  and  $\sigma^-$  polarized light. The atoms are prepared in the  $m_j = -8$  state so only the  $\sigma^-$  light couples to the atoms. This leads to a density-dependent phase shift with of the  $\sigma^-$  polarization with respect to the  $\sigma^+$  one. A polarizer converts this phase shift to an intensity modulation of the light. To have the imaging laser in the direction of the magnetic field in all measurements, the magnetic field is turned in z-direction within 200  $\mu$ s before taking the pictures.

### 6.3 Rotating Quantum Droplets

In the previous chapters we have described the experimental setup that allows us to change the direction of the magnetic field and finally see how the droplets behave. Before experimenting with the new coils, we performed preliminary experiments with a rotating magnetic field using the current setup.

At the 1 G Feshbach resonance it is possible to apply a magnetic field in all directions. In the light sheet there is a strong confinement along  $z$  with  $f_z = 900$  Hz and weaker transversal confinement of  $f_{x,y} \approx 40$  Hz.

In this trap a BEC is stable with a magnetic field pointing in the  $z$ -direction. With tilting the field into the  $xy$ -plane the DDI gets more attractive than repulsive and therefore the overall interaction also becomes attractive. This leads to a collapse and the formation of the droplet. Due to the use of the 1 G Feshbach resonance only small droplets with around 1000 atoms are possible. This is near the critical number of around 600 atoms in a single droplet so they are not deep in self-bound regime and cannot live long without the traps.

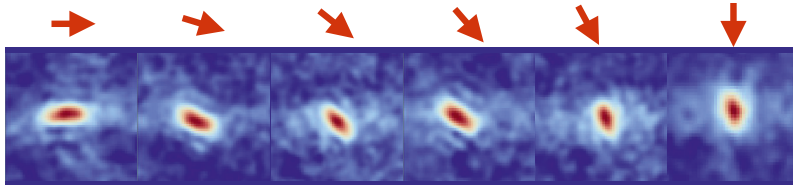


Figure 21: Phase-contrast images of a single droplet taken at different times in a rotating magnetic field. It can be seen that the droplet follows the field nicely.

The droplets are elongated and aligned in the direction of the magnetic field (see figure 21). Naively, one would expect a droplet to have a large dipole  $\boldsymbol{\mu}$  such that when the field is not aligned with the droplet, it starts precessing due to the torque  $\boldsymbol{\tau} = \boldsymbol{\mu} \times \mathbf{B}$ . However this is not the case: each atom has a Larmor frequency much higher than the field rotation frequency. In consequence they instantaneously follow the field. The rotation of the droplet then comes from the force that the atoms create on each other due to the DDI. The alignment of the atoms along the magnetic field is necessary for the binding of the droplet, thus the droplet follows the field in order to minimize energy.

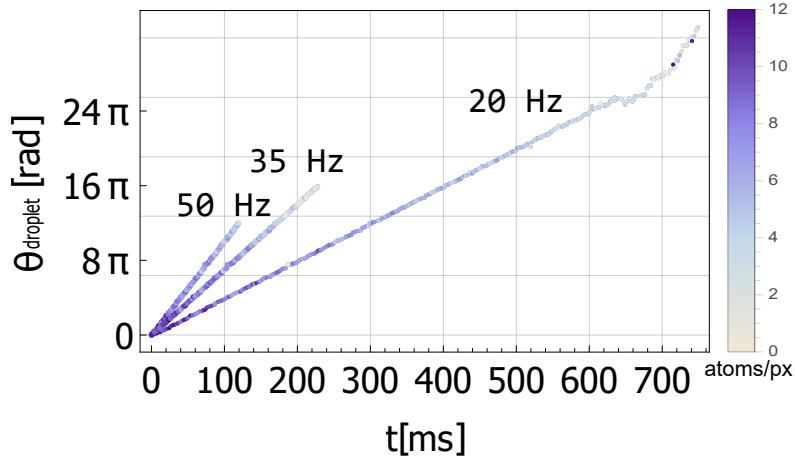


Figure 22: Rotating angle over the time, for a magnetic field rotating at 20, 35 and 50 Hz. With the time the atom number decreases, meaning there are less atoms. And the radial trap frequency in this case is about 35 Hz.

In figure 22 the angle of a droplet over the time is shown and there is no delay between the droplets and the applied magnetic field. During the time  $t$  of the rotation we lose atoms inside the droplet due to three-body loss and as such the atom number per pixel decreases. With higher frequencies the droplets lose the atoms faster and therefore the lifetime decreases. With this also less turns are possible. The rotation of the droplets leads to centrifugal forces at the atoms. Because of this there is an effective potential consisting of the trap potential, the potential due to the binding of the droplets and the centrifugal potential. Higher frequencies lowers the depth of effective potential, so that more atoms leave the droplets.

In figure 23 the lifetimes of the droplets for different rotation frequencies of the magnetic field are shown. It seems that the droplets can rotate faster than the radial trap frequencies. In a purely contact-interacting gas the atoms are not trapped while rotating faster than the trap frequency. The higher frequencies show the self-bound character of the droplets. Although there is a step in the lifetime between 20 and 30 Hz from 600 ms to below 200 ms. With low frequencies the rotation seems to have no effect of the lifetime.

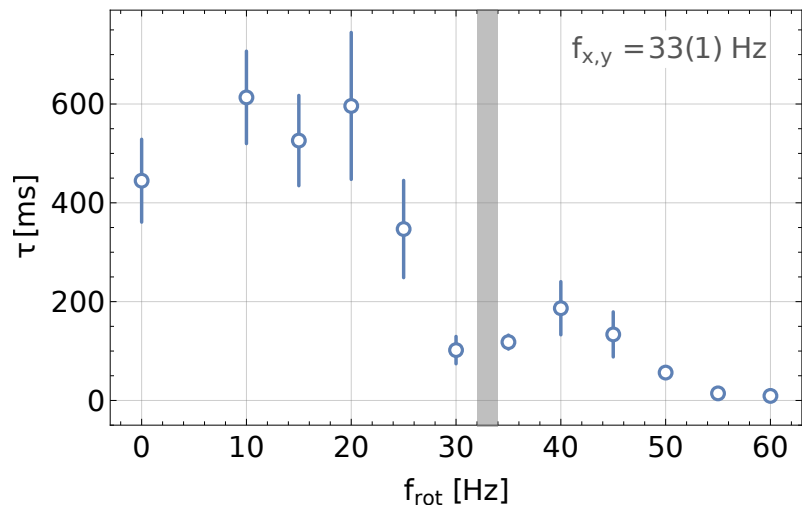


Figure 23: Lifetime of the droplet while rotating the magnetic field at different frequencies. The gray bar shows the trap frequencies  $f_{x,y}$  in radial direction.

## 7 Summary and Outlook

Within this thesis a new setup of coils was built to enable the tuning of the contact interaction as well the DDI. This new setup allows to apply the magnetic field in any direction at a field strength of up to 8 G with the possibility to rotate it quickly, which is necessary to tune the dipolar interaction. For the fast rotation of the magnetic field a LCR circuit with a resonance frequency of 5 kHz is needed. This was successfully tested, as shown in chapter 4.2. The scattering length close to the Feshbach resonance at 7.12 G, with a width of 51 mG, is better controllable than the narrower one at 1.32 G (width 8 mG) that was used for the recent experiment [35] as well as the ones shown here. In practice, this should lead to higher atom numbers of the BEC.

The new setup of the coils was recently implemented in the experiment. The next step is to calibrate the coils by radio frequency spectroscopy directly at the position of the atoms.

With the higher atom number the observation of vortices in dipolar gases may be possible. This is interesting because simulations show anisotropic vortices when tilting the field. In such a configuration vortex arrays should align in a linear stripes in contrast to the well-known Abrikosov lattices.

With the tuning of the DDI interesting measurements will become possible. In dysprosium the scattering length is not known well, since measurements with thermal atoms [41, 42] and measurements in the droplet phase show clear deviations [12]. A possible explanation is the dependence of the effective DDI on the collisional energy, as predicted in [48].

By tuning the DDI to zero the scattering length could be measured allowing to see if this prediction is valid. However, since the tuning of the DDI has never been done before experimentally it first needs to be verified that this method actually works. Also, the form of the droplets should dramatically change with the sign of the dipole-dipole interaction. While they are elongated in the attractive case considered so far, repulsive interactions should instead lead to a pancake like form.

Another interesting future research area is quantum magnetism [38, 39], where the evolution of spins on a lattice is studied. For this purpose, very low magnetic fields are necessary. Therefore a magnetic shielding made of mu-metal was tested in

this thesis. We confirmed that a box has a higher shielding effect than a single plate. For the tested single layer of 0.1 mm we achieved a shielding ratio of up to 20. Holes in such a mu-metal box are necessary for optical access. Their effect was found to be weak if the atoms are further away from a hole than its diameter. In order to apply well-controlled magnetic fields inside the box coils in a Helmholtz configuration are not optimal, because the magnetic field is disturbed by the surrounding box and not very homogeneous. If the coils are placed far away from the mu-metal, this effect becomes negligible.

This experiment with dysprosium BEC and droplets makes interesting phenomena with dipolar interaction and beyond-mean-field theory accessible. Exemplary, the behavior of quantum droplets in a rotating magnetic field was shown in this thesis. The droplet follows the magnetic field with almost no delay. The lifetime of such droplets is not affected by slow rotation and is shortened when the xy-trap-frequencies are approached. This can be used as a probe for collective oscillations of the atoms [43]. The new setup allows for a faster rotation of the magnetic field. This might be a feasible way to measure the binding energy in the droplet.

## Danksagung

Prof. Tilman Pfau möchte ich dafür danken, dass er mir ermöglicht hat im 5. Physikalischen Institut diese Masterarbeit zu schreiben. Danken möchte ich vor allem dem genialen Dysprosium Team. Matthias Wenzel, Fabian Böttcher Michael Eisenmann, Tim Langen und vor allem Igor Ferrier-Barbut. Es war toll mit euch zu arbeiten und Vielen Dank, dass ihr auch manche dumme Frage beantwortet habt und viele Stunden mit Korrigieren verbracht habt.

Vielen Dank dem gesamten 5. Physikalischen Institut

Mein besonderer Dank gilt meinen Freunden und Kommilitonen, Moritz Hirschmann, Kai Langnau und Josephine Gutekunst für das Korrekturlesen und die moralische Unterstützung.

Und vor allem gilt der Dank meinen Eltern, ohne deren persönlichen und finanziellen Unterstützung das ganze Studium nie möglich gewesen wäre.

## **Eidesstattliche Erklärung**

Ich versichere, die Masterarbeit selbstständig und lediglich unter Benutzung der angegebenen Quellen und Hilfsmittel verfasst zu haben.

Ich erkläre weiterhin, dass die vorliegende Arbeit noch nicht im Rahmen eines anderen Prüfungsverfahrens eingereicht wurde.

Carl Matthias Bühner

Stuttgart, den 17. November 2017

## References

- [1] K. B. Davis, M. O. Mewes, M. R. Andrews, N. J. van Druten, D. S. Durfee, D. M. Kurn, and W. Ketterle, “Bose-Einstein Condensation in a Gas of Sodium Atoms”, *Phys. Rev. Lett.* **75**, 3969 (1995).
- [2] M. H. Anderson, J. R. Ensher, M. R. Matthews, C. E. Wieman, and E. A. Cornell, “Observation of Bose-Einstein Condensation in a Dilute Atomic Vapor”, *Science* **269**, 198 (1995).
- [3] D. J. Wineland and W. M. Itano, “Laser cooling of atoms”, *Phys. Rev. A* **20**, 1521 (1979).
- [4] W. Ketterle and N. V. Druten, in , Vol. 37, edited by B. Bederson and H. Walther, *Advances In Atomic, Molecular, and Optical Physics Supplement C* (Academic Press, 1996), pp. 181–236.
- [5] S. Stellmer, M. K. Tey, B. Huang, R. Grimm, and F. Schreck, “Bose-Einstein Condensation of Strontium”, *Phys. Rev. Lett.* **103**, 200401 (2009).
- [6] A. Griesmaier, J. Werner, S. Hensler, J. Stuhler, and T. Pfau, “Bose-Einstein Condensation of Chromium”, *Phys. Rev. Lett.* **94**, 160401 (2005).
- [7] M. Lu, N. Q. Burdick, S. H. Youn, and B. L. Lev, “Strongly Dipolar Bose-Einstein Condensate of Dysprosium”, *Phys. Rev. Lett.* **107**, 190401 (2011).
- [8] K. Aikawa, A. Frisch, M. Mark, S. Baier, A. Rietzler, R. Grimm, and F. Ferlaino, “Bose-Einstein Condensation of Erbium”, *Phys. Rev. Lett.* **108**, 210401 (2012).
- [9] J. Stuhler, A. Griesmaier, T. Koch, M. Fattori, T. Pfau, S. Giovanazzi, P. Pedri, and L. Santos, “Observation of Dipole-Dipole Interaction in a Degenerate Quantum Gas”, *Phys. Rev. Lett.* **95**, 150406 (2005).
- [10] S. Giovanazzi, A. Görlitz, and T. Pfau, “Tuning the dipolar interaction in quantum gases”, *Physical Review Letters* **89**, 130401 (2002).
- [11] H. Kadau, M. Schmitt, M. Wenzel, C. Wink, T. Maier, I. Ferrier-Barbut, and T. Pfau, “Observing the Rosensweig instability of a quantum ferrofluid”, *Nature* **530**, 194 (2016).
- [12] M. Schmitt, M. Wenzel, F. Böttcher, I. Ferrier-Barbut, and T. Pfau, “Self-bound droplets of a dilute magnetic quantum liquid”, *Nature* **539**, 259 (2016).
- [13] H. K. Onnes, “Nobel lecture: Investigations into the properties of substances at low temperatures, which have led, amongst other things, to the preparation of liquid helium”, (1913).
- [14] P. Kapitza, “Viscosity of liquid helium below the  $\lambda$ -point”, *Nature* **141**, 74 (1938).

- [15] A. D. Allen J. F. and Misener, “Flow of liquid helium II”, *Nature* **141**, 75 (1938).
- [16] S. L. Cornish, N. R. Claussen, J. L. Roberts, E. A. Cornell, and C. E. Wieman, “Stable  $^{85}\text{Rb}$  Bose-Einstein Condensates with Widely Tunable Interactions”, *Phys. Rev. Lett.* **85**, 1795 (2000).
- [17] C. C. Bradley, C. A. Sackett, J. J. Tollett, and R. G. Hulet, “Evidence of Bose-Einstein Condensation in an Atomic Gas with Attractive Interactions”, *Phys. Rev. Lett.* **75**, 1687 (1995).
- [18] G. Modugno, G. Ferrari, G. Roati, R. J. Brecha, A. Simoni, and M. Inguscio, “Bose-Einstein Condensation of Potassium Atoms by Sympathetic Cooling”, *Science* **294**, 1320 (2001).
- [19] T. Weber, J. Herbig, M. Mark, H.-C. Nägerl, and R. Grimm, “Bose-Einstein Condensation of Cesium”, *Science* **299**, 232 (2003).
- [20] J. Stuhler, A. Griesmaier, J. Werner, T. Koch, M. Fattori, and T. Pfau, “Ultracold chromium atoms: from Feshbach resonances to a dipolar Bose-Einstein condensate”, *Journal of Modern Optics* **54**, 647 (2007).
- [21] L. Pitaevskii and S. Stringari, *Bose-Einstein Condensation*, International Series of Monographs on Physics (Clarendon Press, 2003).
- [22] T. Koch, T. Lahaye, J. Metz, B. Fröhlich, A. Griesmaier, and T. Pfau, “Stabilization of a purely dipolar quantum gas against collapse”, *Nature physics* **4**, 218 (2008).
- [23] T. Lahaye, J. Metz, B. Fröhlich, T. Koch, M. Meister, A. Griesmaier, T. Pfau, H. Saito, Y. Kawaguchi, and M. Ueda, “*D*-Wave Collapse and Explosion of a Dipolar Bose-Einstein Condensate”, *Phys. Rev. Lett.* **101**, 080401 (2008).
- [24] I. Ferrier-Barbut, H. Kadau, M. Schmitt, M. Wenzel, and T. Pfau, “Observation of Quantum Droplets in a Strongly Dipolar Bose Gas”, *Phys. Rev. Lett.* **116**, 215301 (2016).
- [25] D. S. Petrov, “Quantum Mechanical Stabilization of a Collapsing Bose-Bose Mixture”, *Phys. Rev. Lett.* **115**, 155302 (2015).
- [26] D. Baillie, R. M. Wilson, R. N. Bisset, and P. B. Blakie, “Self-bound dipolar droplet: A localized matter wave in free space”, *Phys. Rev. A* **94**, 021602 (2016).
- [27] F. Wächtler and L. Santos, “Ground-state properties and elementary excitations of quantum droplets in dipolar Bose-Einstein condensates”, *Phys. Rev. A* **94**, 043618 (2016).
- [28] S. Götz, “Demagnetization cooling in an ultracold chromium gas”, Diplom thesis (Pi5 Universität Stuttgart, 2006).

- [29] W. Demtröder, *Experimentalphysik 2*, Experimentalphysik / Wolfgang Demtröder (Springer Berlin Heidelberg, 2009).
- [30] C. Gerthsen and D. Meschede, *Gerthsen Physik*, Springer-Lehrbuch (Springer, 2003).
- [31] S. Müller, “Stability and collapse dynamics of dipolar Bose-Einstein condensates in one-dimensional optical lattices”, PhD thesis (2013).
- [32] C. Chin, R. Grimm, P. Julienne, and E. Tiesinga, “Feshbach resonances in ultracold gases”, *Rev. Mod. Phys.* **82**, 1225 (2010).
- [33] T. D. Lee, K. Huang, and C. N. Yang, “Eigenvalues and Eigenfunctions of a Bose System of Hard Spheres and Its Low-Temperature Properties”, *Phys. Rev.* **106**, 1135 (1957).
- [34] T. Maier, “Interactions in a Quantum Gas of Dysprosium Atoms”, PhD thesis (Pi5 Universität Stuttgart, 2015).
- [35] M. Wenzel, F. Böttcher, T. Langen, I. Ferrier-Barbut, and T. Pfau, “Striped states in a many-body system of tilted dipoles”, (2017).
- [36] J. Simpson, J. Lane, C. Immer, and R. Youngquist, “Simple Analytic Expressions for the Magnetic Field of a Circular Current Loop”, (2003).
- [37] M. Wenzel, “Aktive Magnetfeldkompensation für atomoptische Experimente”, Bachelor thesis (Pi5 Universität Stuttgart, 2012).
- [38] B. Naylor, E. Maréchal, J. Huckans, O. Gorceix, P. Pedri, L. Vernac, and B. Laburthe-Tolra, “Cooling of a Bose-Einstein Condensate by Spin Distillation”, *Phys. Rev. Lett.* **115**, 243002 (2015).
- [39] A. de Paz, A. Sharma, A. Chotia, E. Maréchal, J. H. Huckans, P. Pedri, L. Santos, O. Gorceix, L. Vernac, and B. Laburthe-Tolra, “Nonequilibrium Quantum Magnetism in a Dipolar Lattice Gas”, *Phys. Rev. Lett.* **111**, 185305 (2013).
- [40] *Magnetische Abschirmungen*, Grundlagen, Lieferprogramm, Messtechnik, Sekels GmbH ().
- [41] Y. Tang, A. Sykes, N. Q. Burdick, J. L. Bohn, and B. L. Lev, “*S*-wave scattering lengths of the strongly dipolar bosons  $^{162}\text{Dy}$  and  $^{164}\text{Dy}$ ”, *Phys. Rev. A* **92**, 022703 (2015).
- [42] T. Maier, I. Ferrier-Barbut, H. Kadau, M. Schmitt, M. Wenzel, C. Wink, T. Pfau, K. Jachymski, and P. S. Julienne, “Broad universal Feshbach resonances in the chaotic spectrum of dysprosium atoms”, *Phys. Rev. A* **92**, 060702 (2015).
- [43] I. Ferrier-Barbut, M. Wenzel, F. Böttcher, T. Langen, and T. Pfau, “Scissors Mode in Quantum Droplets”, in preperation.

- [44] T. Maier, H. Kadau, M. Schmitt, A. Griesmaier, and T. Pfau, “Narrow-line magneto-optical trap for dysprosium atoms”, *Opt. Lett.* **39**, 3138 (2014).
- [45] K. Goral and L. Santos, “Ground state and elementary excitations of single and binary Bose-Einstein condensates of trapped dipolar gases”, **66** (2002).
- [46] M. Wenzel, “A dysprosium quantum gas in highly controllable optical traps”, Master thesis (Pi5 Universität Stuttgart, 2015).
- [47] V. J. Fowler and J. Schlafer, “A Survey of Laser Beam Deflection Techniques”, *Appl. Opt.* **5**, 1675 (1966).
- [48] R. Ołdziejewski and K. Jachymski, “Properties of strongly dipolar Bose gases beyond the Born approximation”, *Phys. Rev. A* **94**, 063638 (2016).